Equilibrium and dynamics of single-peptide binding to aluminum oxides: Emphasizing the role of local surface charge and hydrophobicity

Autorías no ditellianas: Lê-Chesnais, Joanne; Méthivier, Christophe; Humbert, Cristophe; Lambert, Jean-Francois; Landoulsi, Jessem

Autoría ditelliana: Rodríguez, Daniela

Fecha de publicación: 11/09/2025

Publicado originalmente en: Applied Surface Science Advances (ISSN 2666-5239)

Applied Surface Science Advances 29 (2025) 100840

Contents lists available at ScienceDirect

Applied Surface Science Advances

journal homepage: www.sciencedirect.com/journal/applied-surface-science-advances

Full Length Article

Equilibrium and dynamics of single-peptide binding to aluminum oxides: Emphasizing the role of local surface charge and hydrophobicity

Joanne Lê-Chesnais [a], Christophe Méthivier [a], Daniela Rodriguez [b], Christophe Humbert [c], Jean-François Lambert [d,*], Jessem Landoulsi [a,*]

[a] Sorbonne Université, CNRS, Laboratoire de Réactivité de Surface, 4 Place Jussieu, F-75005, Paris, France
[b] CONICET, Departamento de Matematicas y Estadistica, Universidad T. Di Tella, Av.Q3 Figueroa Alcorta 7350 (1428), Buenos Aires, Argentina
[c] Institut de Chimie Physique, Université Paris-Saclay, CNRS, UMR8000, 91405 Orsay, France
[d] Sorbonne Université, CNRS, Laboratoire d'Archéologie Moléculaire et Structurale, 4 Place Jussieu, F-75005, Paris, France

ARTICLE INFO

Keywords:
Single-molecule
Surface charge
Hydrophobicity
Atomic force microscopy
X-ray photoelectron spectroscopy
Origins of life

ABSTRACT

Understanding the interactions between biomolecules and mineral surfaces is a fundamental challenge at the crossroads of colloid science, surface chemistry, and molecular biophysics. While peptides and amino acids are known to bind a variety of metal oxides, our understanding remains limited regarding how local surface characteristics influence these interactions at the nanoscale. This is particularly important for "real surfaces" which intrinsically exhibit heterogenous features that determines their behavior when interacting with biomolecules. Herein, we present a fresh perspective that focuses on probing local surface properties and dipeptide (Glu-Ala) binding on oxides grown on polycrystalline aluminum metal at the single-molecule level. First, a comprehensive surface characterization is performed to resolve the chemical composition and topography of two different native aluminum oxide surfaces. Then, by using atomic force microscopy (AFM) in force spectroscopy mode, we employ chemical force microscopy and colloidal probe techniques to quantify local surface charge and hydrophobicity, revealing noticeable differences between the two studied surfaces. Our findings demonstrate that both free enthalpies of adsorption ($\Delta_{ads}G^{\circ}$) and kinetic unbinding rates (k_{off}) are highly influenced by the surface characteristics probed locally, and suggest that the interaction of the dipeptide with the surfaces is dominated by van der Waals and hydrogen bonding. Beyond these fundamental insights regarding peptide–mineral interactions, this work provides methodological developments that are relevant for exploring molecular recognition mechanism, particularly on "real" oxide surfaces. Additionally, the implications of our findings extend to the design of peptide-functionalized materials and offer new perspectives on surface-mediated prebiotic chemistry, potentially relevant to the emergence of life on early Earth.

1. Introduction

Oligopeptides, i.e. short chains of amino acids, exhibit a remarkable capacity to interact with various inorganic surfaces including metals, oxides and other minerals. Interfacial processes involved between oligopeptides and these mineral surfaces play a key role in promising fields including the regulation of cell-material interactions [1,2] or biomineralization [3–6]. They are also of high significance in the context of the origins of life, as mineral surfaces have been proposed as plausible sites for peptide bond formation, a fundamental step in prebiotic chemistry on the early Earth, facilitating amino acid condensation and thus leading to the formation of the first biopolymers [7–12]. To investigate this hypothesis, studies have examined amino acid polymerization on various mineral surfaces (clays, silica, Al and Ti oxides, pyrite…), which serve as analogs for primitive Earth minerals. Although clays are among the most geologically relevant and abundant minerals on the primitive Earth, experimental studies have repeatedly shown that metal oxides such as silica and alumina are often more effective in promoting condensation reactions between amino acids [13–18]. Indeed, the surface reactivity of these stoichiometrically simple oxides is significantly different from that of clay minerals, involving in particular a pH dependent surface charge. Moreover, the widespread interest in aluminum oxide materials may be explained both by the abundance of aluminum in Earth's crust and its proposed presence as alumina in

* Corresponding authors.
E-mail addresses: jean-francois.lambert@sorbonne-universite.fr (J.-F. Lambert), jessem.landoulsi@sorbonne-universite.fr (J. Landoulsi).

https://doi.org/10.1016/j.apsadv.2025.100840
Received 27 June 2025; Received in revised form 24 August 2025; Accepted 30 August 2025
Available online 11 September 2025

interstellar dust by Hazen [19]. Despite this relevance, studies on aluminum oxide in prebiotic polymerization and adsorption [14,20–26] remain scarce compared to silica, underscoring the need to explore its role in surface-mediated prebiotic processes.

Understanding the surface reactions necessitates to study the interaction with mineral surfaces, not only of the starting amino acids, but also of the peptides that are formed by condensation and can also undergo further reactions, or be desorbed.

Metal oxide surfaces exhibit different types of chemical structures – oxides, hydroxides and oxyhydroxides – when submitted to different conditions of temperature, or exposed to different media [27,28]. Their crystal structure, morphology and composition, can be directly linked to their chemical and catalytic properties [29–31]. Thus, these surfaces are widely studied in the literature, but most of the studies conducted in catalysis and biointerfaces fields have been devoted to stable and highly ordered oxides such as specific facets of monocrystals. While model surfaces can be extremely useful in various contexts, they often fail to reflect the "real surfaces" encountered in natural environments, whether in the field of biomaterials or prebiotic chemistry. "Real surfaces" exhibit intrinsic heterogenous characteristics, including multiple crystalline phases, varied orientations, structural defects, and irregularities, all of which significantly impact their behavior especially when interacting with biomolecules in aqueous environments [32]. These complexities involve multiple interfacial processes such as dissolution, oxidation, and the ubiquitous adsorption of organic contaminants, which differ markedly from those observed on idealized model surfaces and therefore cannot be adequately represented by model systems alone. One way to explore this concept of "real surfaces" can be achieved through the study of oxides grown on polycrystalline metallic materials. Indeed, for passive metals such as aluminum, this leads to the formation of a thin oxide layer, typically only a few nanometers thick, exhibiting heterogenous features and undergoing continuous transformation due to simultaneous dissolution and regeneration processes.

Characterizing a highly heterogeneous surface and its interaction with a biomolecule requires local-scale measurements of (i) the properties of the surface and the solid/liquid interface it forms, and (ii) the biomolecule's interaction with the surface. Both of these requirements can be achieved by applying atomic force microscopy (AFM) in its force spectroscopy mode, thanks to the significant developments made in the functionalization of AFM tips. First, chemical force microscopy and colloidal probe may, indeed, investigate local surface hydrophobicity and charge at the nanoscale. Second, the single-molecule force spectroscopy (SMFS) approach may explore different interaction modes that are not always accessible with ensemble-average measurements [33–38].

The progresses made in the manipulation of individual biological receptors by AFM have been particularly beneficial in probing peptide/mineral interfaces at the single-molecule level [28,39–43]. SMFS has been extensively used to extract kinetic and thermodynamic parameters of the probed interactions, thanks to the development of various models. Particularly, dynamic force spectroscopy experiments allow to draw a relationship between the unbinding force and the loading rate at which the bond is broken. From these measurements, directly probing unbinding events, dissociation kinetic constants of the interaction can be estimated [44,45]. Significant efforts have also been made in both conceptual and experimental approaches to extract thermodynamic parameters of the interaction such as the free enthalpy of adsorption $\Delta_{ads}G^{\circ}$ [46,47] including previous work from our team [48]. Specifically, exploring the thermodynamic and kinetic parameters of peptide-oxide interactions is relevant in prebiotic chemistry, as adsorption must strike a balance, too strong leads to irreversible binding, too weak prevents sufficient retention for further reactions.

While SMFS studies usually emphasize the role of the peptide, including the size of the residue [43], its polarity [49], or the effect of amino acid substitution [50], the surface heterogeneity in itself is often neglected. This is a shortcoming because in the case of metal oxides, the surface reactivity may greatly influence the adsorption behavior of oligopeptides and *vice versa* [51,52].

In the present work, we investigate, at the single-molecule level, the interaction of a small oligopeptide with two aluminum oxide surfaces, either native – i.e. grown from the underlying polycrystalline metallic substrate at room temperature – or exposed to a thermal annealing process. Our study broadly investigates how a biomolecule interacts with metal oxides that exhibit different chemical and physical properties. More specifically, it examines how chemical transformations of aluminum oxides, expected under varying thermal conditions on early Earth, influence surface properties and thereby peptide interactions. The dipeptide Glu–Ala was chosen for both prebiotic plausibility and experimental relevance. Glutamic acid and alanine are consistently produced in high yields under simulated prebiotic conditions (interstellar ice analogues, atmospheric discharge, hydrothermal systems) and are abundant in carbonaceous meteorites, suggesting availability on early Earth [53]. Moreover, we have previously observed that the Glu + Ala amino acids system, like Glu + Leu [17,18], can form long, prebiotically relevant linear oligopeptides [54].

First, a thorough analysis of the chemical composition and topography of the prepared aluminum oxide surfaces was made using a wide range of surface characterization techniques. Such extensive analysis is essential, as the oxide surfaces used in this study are structurally and chemically different from those most often used in the literature, such as single-crystal α-Al_2O_3 faces. Then, local measurements of hydrophobicity and surface charge were performed by means of chemical force microscopy and colloidal probe, respectively, to assess the differences in surface properties. Finally, the interaction of both surfaces with a dipeptide (Glu-Ala) were probed by means of SMFS and kinetic and thermodynamic parameters of the interactions were extracted from these measurements. Special attention is given to interpreting these extracted parameters to describe the interaction mechanism of this oligopeptide with surfaces, particularly focusing on how the local surface properties influence this interaction probed at the single-molecule level.

2. Experimental section

2.1. Materials

Chloroform (≥ 99.5%), dimethylsulfoxide (DMSO, ≥ 99.9%), ethanolamine hydrochloride (≥ 99%), triethylamine (≥ 99.5%), sodium cyanoborohydride ($NaCNBH_3$, ≥ 95%), ethanolamine (≥ 99%), potassium nitrate (KNO_3, ≥ 99%), 1-undecanethiol (UDT, ≥ 98%) and citric acid (≥ 99%) were purchased from Sigma-Aldrich (France). H-glutamic acid-alanine-OH dipeptide (Glu-Ala, M_w = 218.21 g/mol, ≥ 99%) was purchased from Bachem (France). Acetal-PEG-NHS (Acetal-Polyethylene glycol-*N*-Hydroxysuccinimide) was provided by JKR (Austria). Ethanol (HPLC grade, ≥ 99%) was purchased from VWR (France). Sodium hydroxide (≥ 97%) was purchased from Carlo Erba Reagents (France). All solutions used in this study were prepared in ultrapure water (pH 6.8 ± 0.1, MilliQ, Millipore, France)

2.2. Surface preparation

Polycrystalline aluminum wafers (specimens of 1 cm × 1 cm surface area cut from a 2 mm thick plate, Al 99.99%, Goodfellow, France) were used. Samples were mechanically polished using silicon carbide (SiC) papers of successively 800, 1200 and 4000 grain size on both sides followed by fine polishing with 3 μm diamond suspension (Struers, France). The samples were then rinsed and sonicated (70 W, 40 kHz, USA) in a mixture (50/50%, v/v) of ultrapure water and ethanol and thoroughly rinsed with ultrapure water to ensure the removal of potential polishing material. Finally, the samples were dried under nitrogen gas flow and stored in Petri dishes. These samples are referred to as AlOx since they are superficially oxidized by atmospheric O_2. Some of these wafers were subsequently submitted to thermal annealing under

air at 550°C for 2 hours with a 1°C/min ramp. The thermally annealed wafers were also stored in Petri dishes. They are referred to as T-AlOx. The preparation procedures are illustrated in Fig. 1A below.

2.3. Atomic force microscopy

All AFM experiments, including surface charge measurements and SMFS, were performed using a commercial AFM (NanoScope VIII MultiMode AFM, Bruker Nano Inc- Nano Surfaces Division, USA) and surfaces were fixed to a steel sample puck using double-face tape. Cantilevers used are oxide-sharpened microfabricated Si_3N_4 purchased from Bruker Nano Inc., Nano Surfaces Division, USA. The spring constants of the cantilevers were measured using the thermal noise method.

Imaging. AFM images were recorded in the Peak Force Tapping© mode. The spring constants of the cantilevers were in the 0.3 to 0.8 N/m range and the curvature radius of the tip was less than 10 nm (manufacturer specifications).

Chemical force microscopy. Experiments were performed using a Au/Cr coated silicon nitride AFM tip. The tip was functionalized using the following procedure. AFM tips were placed in an UV–ozone cleaner for 30 min and immerged in a 1 mM UDT solution in absolute ethanol for 16 hours. The obtained AFM tips were rinsed for 5 minutes in absolute ethanol then in ultrapure water. All hydrophobic measurements were performed in ultrapure water in the liquid cell. The spring constant of the cantilevers was in the 0.04 to 0.06 N/m range and the curvature radius of the tip was about 60 nm (manufacturer specifications).

Colloidal probe. AFM surface charge measurements were performed using oxidized silicon nitride colloidal probes in the liquid cell. The colloidal probes were purchased from Bruker (Nano Inc., Nano Surfaces Division, USA). The spring constant of the cantilevers was in the 0.03 to 0.06 N/m. The curvature radius of the colloidal probes was 1 μm (manufacturer specifications). Surface charge measurements were performed in a fresh 10^{-5} M KNO_3 solution adjusted to pH 6.8 ± 0.1 with 0.1 M NaOH. 100 μL of the solution were deposited on the surface, the AFM tip was approached to the surface and left to equilibrate for 10 to 15 min before measurements.

Single-molecule force spectroscopy measurements (SMFS). SMFS measurements were performed using several cantilevers with spring constants ranging from 0.09 to 0.5 N/m. All force measurements were recorded at a loading rate (r) range of 3.10^4 to 2.10^7 pN/s. The r values were calculated by multiplying the spring constant of the cantilever by its retraction rate.

AFM tips were functionalized with H-Glutamyl-Alanine-OH (Glu-Ala) dipeptide using an acetal-PEG-NHS heterobifunctional linker following the protocol developed by Gruber et al. [55]. Cantilevers were placed in an UV–ozone cleaner for 30 min, rinsed with chloroform and absolute ethanol, and immersed overnight in an ethanolamine hydrochloride solution (13.2 g in 26.4 mL of DMSO). They were washed 3

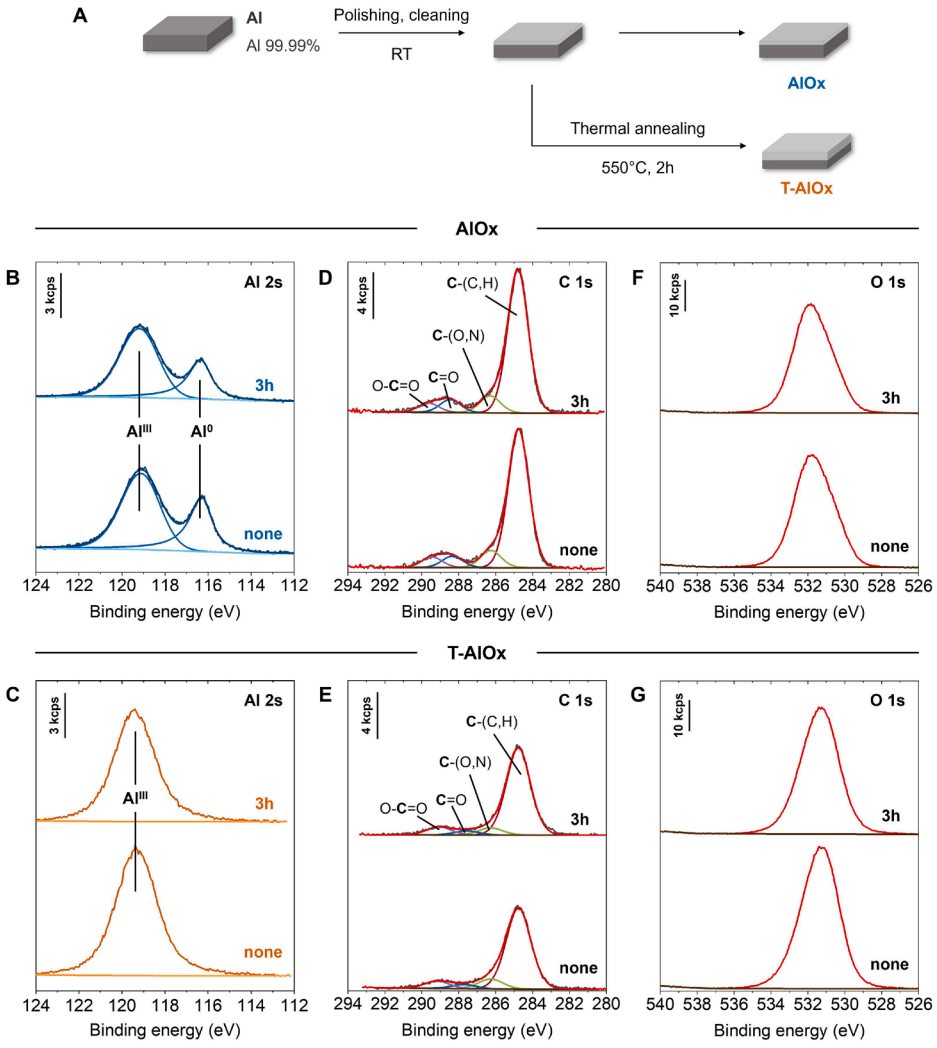

Fig. 1. (A) Procedure used for the preparation of AlOx and T-AlOx surfaces. (B,C) Al 2s, (D,E) C 1s and (F,G) O 1s XPS peaks recorded on AlOx and T-AlOx surfaces prior to ("none") and after incubation in water for 3 h.

times with DMSO and 3 times with absolute ethanol, then dried with nitrogen. The obtained cantilevers were immersed 2 hours into a linker solution prepared by dissolving 1 mg of acetal-PEG-NHS in 0.5 mL of chloroform and 10 µl of triethylamine, washed 3 times in chloroform and dried under nitrogen. Linker-modified cantilevers were immersed 10 min into a 1% citric acid solution, washed 3 times with ultrapure water and dried under nitrogen. They were then placed in a 100 µL drop of the dipeptide solution (0.1 mg/mL) to which 2 µL of $NaCNBH_3$ 1 M were added. After 1 hour, 5 µL of 1 M ethanolamine at pH 8 were added. Cantilevers were left to incubate for 10 more minutes, then washed 3 times, and stored in ultrapure water for a maximum of 1 week before use.

2.4. Attenuated Total Reflection-Fourier Transformation Infrared (ATR-FTIR)

ATR-FTIR measurements were carried out using an FTIR spectrometer (Bruker, VERTEX 80) equipped with a mono-reflection diamond (refractive index of 2.4) ATR device (Bruker, A225/Q-DLST). Radiation from the spectrometer IR source was focused on the ATR crystal and the output radiation (on the other side of the crystal) was focused on a liquid nitrogen-cooled MCT (mercury cadmium telluride) detector (Bruker, D316-L/B). Measurements were performed in the 550–7800 cm^{-1} spectral range under RapidScan Mode, with a mirror speed of 160 kHz. Each spectrum was the sum of 250 scans. In this study, the aluminum oxide surfaces were placed face down against the diamond crystal and held with a pressure point. The background was recorded in ambient conditions of pressure and temperature with no sample pressed against the crystal.

2.5. X-ray photoelectron spectroscopy (XPS)

XPS analyses were performed using a SPECS (Phoibos 100-1D-DLD) spectrometer (SPECS, Germany) equipped with a monochromatized aluminum X-ray source ($h\nu = 1486.6$ eV) powered at 16 mA and 14 kV. The resulting analyzed area was about 1 mm in diameter. A pass energy of 100 eV was used for survey scan and 20 eV for narrow scans. In the latter conditions, the full width at half maximum (FWHM) of the Ag $3d_{5/2}$ peak of a standard silver sample was about 0.6 eV. Aluminum samples were fixed on the metallic support, and no charge stabilization device was used on these conducting samples. The pressure in the analysis chamber during measurement was 10^{-10} Torr. The photoelectron collection angle, θ, between the normal to the sample surface and the analyzer axis was 0°. The following sequence of spectra was recorded: survey spectrum, C 1s, O 1s, Al 2s and Al 2p. XPS peaks were referenced to the C 1s peak of carbon bound to only carbon and hydrogen at 284.8 eV. The data treatment was performed with CasaXPS software (Casa Software Ltd, U.K.) [56]. The peaks were decomposed using a U 2 Tougaard baseline and a Voigt line shape. Molar concentration ratios were calculated using peak areas normalized according to Scofield factors.

2.6. Sum-frequency generation (SFG)

SFG spectroscopy was performed on the samples at the Institut de Chimie Physique using a homemade setup based on a pulsed IR laser from Quantel-Laser (Nd:YAG,1064, 12 ps) described elsewhere [57]. After an amplification stage, the laser source pumps two optical parametric oscillators (OPO). The infrared OPO is tunable over the 3040–3840 cm^{-1} spectral range of the OH stretching vibration modes, while the visible one is fixed at 532 nm. The tunable IR and the fixed visible laser beams are coherently mixed at the same point of the probed sample surface at 65° and 55° incidence angles with respect to the surface normal direction, respectively. The polarization scheme is either ppp or ssp for the SFG, visible, and IR beams. The SFG beam is therefore collected by a photomultiplier after spatial and spectral filtering through a double-stage monochromator. SFG data were normalized by the IR and visible beam powers for each wavelength to compensate for potential laser sources' power fluctuations. The frequency resolution of the infrared OPO is equal to 3 cm^{-1} as set by an etalon plate.

2.7. Models

Surface charge. When a metal oxide is immersed in an electrolyte, a charged interface forms as a result of the dissociation of the surface chemical groups and the adsorption of ions. The organization of ions at the interface leads to the formation of an electrical double layer (EDL), which has been described by several models [58–60] and can be considered as being composed of (i) a compact layer of ions bearing a charge opposite to that of the surface (Stern layer) and (ii) a diffuse region of mobile ions across the medium, until reaching the bulk electrolyte where no local variation of the electrical potential can be observed. Probing the EDL provides access to the surface charge of the underlying substrate, which is governed by the chemical composition of the surface groups and their capacity to protonate or deprotonate when immersed in liquid. When a colloid is approached to a surface in an electrolyte medium, the total force as a function of distance $F(d)$, resulting from the addition of van der Waals forces and electrostatic interactions between the electric double layers, can be plotted according to the Derjaguin–Landau–Verwey–Overbeek (DLVO) model [61,62]. This model describes the interaction of double layers at constant charge boundary conditions as:

$$\frac{F(d)}{R} = \frac{2\pi\varepsilon_r\varepsilon_0}{\varkappa^{-1}}\left[2\psi_{SiO_2}\psi_{Surf}exp^{-d/\varkappa^{-1}} + \left(\psi^2_{SiO_2} + \psi^2_{Surf}\right)exp^{-2d/\varkappa^{-1}}\right] - \frac{H}{6d^2} \quad (1)$$

Where R is the effective curvature radius of the colloidal probe (silicon oxide), ε_r the relative dielectric constant of the solution, ε_0 the dielectric constant of vacuum, ψ_{SiO_2} and ψ_{Surf} the surface potentials of SiO_2 and aluminum oxide surfaces (AlOx or T-AlOx), respectively, and H the nonretarded Hamaker constant of the silica/water/surface system. The colloidal probe radius was set at 1 µm, as specified by the manufacturer, ψ_{SiO_2} was fixed at -65 mV based on results obtained from a study conducted on oxidized silicon nitride Si_3N_4 [63] and the Hamaker constant H was set at 1.8×10^{-20} J as for the alumina/water/silica system [64].

To extract the surface potential of AlOx and T-AlOx surfaces using this model, approach F-D curves were collected using force spectroscopy measurements. A total of 1024 F-D curves were fitted with the DLVO model on each surface.

Peptide-surface binding. When probing biomolecule-inorganic surface interactions, the exposed functions of the biomolecule and the surface can be assimilated to a ligand-receptor system that exhibits an association/dissociation equilibrium. Based on this principle, force spectroscopy measurements consist in approaching the biomolecule-functionalized tip to the surface and allowing their interactions. Upon retracting, the rupture of these interactions corresponds to the unbinding event between the biomolecule and the surface. The force needed to unbind the biomolecule from the surface can be measured by AFM force spectroscopy. In many situations, the unbinding force, also commonly called adhesion force F^*_{adh}, was shown to depend on the loading rate at which the bond is broken. This dependance of F^*_{adh} with r was rationalized by the Bell-Evans model [44,45]:

$$F^*_{adh}(r) = \frac{k_B T}{x_t} \times \ln\left(\frac{x_t r}{k_{off} k_B T}\right) \quad (2)$$

where k_B is the Boltzmann constant, T the temperature in Kelvin, and x_t the distance between the bound state and the transition state projected along the applied force direction. By plotting $F^*_{adh}(r)$ and extrapolating the value of the loading rate to zero force ($r_{(F=0)}$), the unbinding rate constant k_{off} can be estimated as:

$$k_{off}(0) = \frac{(r_{F=0})x_t}{k_B T} \quad (3)$$

In the scope of single-molecule measurements as a function of the loading rate, the existence of two distinct stages is frequent [65]. Friddle et al. have proposed a model to explain this trend. They hypothesized that the force spectra profiles do not present a single regime as described by the Bell-Evans model, but rather two distinct regimes [65]: first, a near-equilibrium regime induced by bond rupture and reformation during the retraction of the tip at low loading rates; second, a far-from-equilibrium kinetic regime induced by rapid bond rupture without reformation at high loading rates. In this model, the most probable force F^*_{adh} can be defined as:

$$F^*_{adh}(r) = f_{eq} + \frac{k_B T}{x_t} \ln\left(1 + \frac{e^{-\gamma} r x_t}{k_u k_B T}\right) \quad (4)$$

where γ is the Euler constant. At low loading rates, when r approaches 0, the value of F^*_{adh} converges to f_{eq} which defines the equilibrium force for the ligand-receptor system:

$$F^*_{adh}(r)_{r\to 0} \approx f_{eq} \quad (5)$$

At high loading rates, this model converges to a linear trend:

$$\langle F^*(r)\rangle_{r\to\infty} \approx \frac{k_B T}{x_t} \ln\left(\frac{e^{-\gamma} r x_t}{k_u\left(f_{eq}=0\right) k_B T}\right) \quad (6)$$

Where:

$$k_u\left(f_{eq}=0\right) = \frac{e^{-\gamma} r_{F=0} x_t}{k_B T} \quad (7)$$

Different kinetic parameters can be extracted from Eq. (7) such as the dissociation rate constant k_u or the distance between the bound state and the transition state projected along the applied force direction x_t.

Free enthalpy of adsorption: The standard free energy of adsorption $\Delta_{ads}G^\circ$ is a useful parameter to characterize the binding of biomolecules to inorganic surfaces, and in particular to compare the behavior of the same molecule on different surfaces, as is the case here. Two approaches have been developed over the years to evaluate it from the non-equilibrium SMFS measurements.

(i) The FNDY model, described in detail above, introduces the presence of a minimal force f_{eq} required for the system to escape from the bound state (Eq. 5). This results in the existence of an energy defined as [37]:

$$\Delta_{ads}G^\circ_{FNDY} = k_B T \ln\left(\frac{f_{eq} x_t}{k_B}\right) + f_{eq} x_t + k_B T \quad (8)$$

(ii) The second model is based on the Jarzynski equality and explores the fluctuations of the work performed by a system during a non-equilibrium process to provide an estimate of the free energy difference between the initial and final equilibrium states of the system [46]:

$$e^{-\Delta_{ads}G^\circ_{JE}/k_B T} = < e^{-W_{adh}/k_B T} >_n \quad (9)$$

Where W_{adh} is the work of adhesion. The Jarzynski equality can be adapted to force spectroscopy measurements by considering the work of adhesion W_{adh} as the integral of the adhesion event on a force curve. The equality can thus be expressed as follows:

$$e^{-\Delta_{ads}G^\circ_{JE}/k_B T} = < e^{-\int F\cdot dz / k_B T} >_n \quad (10)$$

The ensemble average indicated by the $\langle . \rangle$ symbol in Eq. 10 is determined from the average of an infinite number of measurements. In practice, the choice of the estimator is a crucial parameter, because it can drastically affect the estimate of the $\Delta_{ads}G^\circ_{JE}$ value from a finite number of measurements. A nonparametric Gamma estimator is relevant to estimate the $\Delta_{ads}G^\circ_{JE}$ from a finite number of measurements [66]. Recently, this estimator has been shown to provide consistent $\Delta_{ads}G^\circ_{JE}$values from SMFS experiments [48,67].

3. Results and discussion

3.1. Chemical composition

The two surfaces referred to as AlOx and T-AlOx were obtained following the procedure described in the experimental part and depicted in Fig. 1A. XPS analysis was performed on both AlOx and T-AlOx surfaces prior to and after incubation in the aqueous solution (pH 6.8 ± 0.1) for 3 h. Typical Al 2s peaks recorded on AlOx surface are shown in Fig. 1B. In this region, two components are observed: one at a binding energy of about 116.5 eV due to metallic aluminum (Al^0) from the underlying substrate and the second one at a higher binding energy, about 119.1 eV, attributed to the oxidized aluminum in the +III oxidation state (Al^{III}). By contrast, only the latter component at about 119.3 eV was observed on the T-AlOx surface (Fig. 1C). The absence of the Al^0 component in this region suggests that the thermal annealing process induced the formation of a thicker aluminum oxide layer on the surface.

The apparent O/Al^{III} molar ratio exhibits significantly higher values for AlOx as compared to T-AlOx (Table 1). However, these values cannot be used as such to probe the chemical composition of the oxides due to two major issues arising from the presence of an adventitious contamination layer, which is unavoidable on high surface energy solids [32]. The first issue relates to the chemical composition of the contamination layer, which primarily consists of hydrocarbon compounds with a proportion of oxidized carbon (see C 1s peak decomposition, Fig. 1D, E). This oxidized carbon accounts for approximately 3 to 10% of the total carbon and contributes to the total oxygen signal (see Section S1.2, Supplementary material). As a result, the measured oxygen includes both inorganic (oxide, hydroxide, adsorbed inorganic ions) and organic components, which impacts the estimation of the O/Al^{III} ratio. A reliable decomposition of the O 1s peak is difficult to achieve due to its featureless shape and the minimal variations observed in the different studied conditions (Fig. 1F, G). The second issue is due to the differential attenuation effect caused by the contamination layer, as aluminum and oxygen have different inelastic mean free paths (Table S1, Supplementary material). This leads to unequal attenuation of their respective signals, further compromising the reliability of the O/Al^{III} molar ratio.

Based on the methodology we previously developed for characterizing bio-organic/inorganic interfaces including metallic surfaces [32] and calcium phosphate minerals [68], we estimated the inorganic fraction of the oxygen (O_{inorg}), while accounting for differential attenuation effects between oxygen and aluminum elements (see section S1.4, Supplementary material). The corrected molar ratios $(O_{inorg}/Al^{III})_{corr}$ are presented in Table 1. On the AlOx surface, the obtained ratio was around 2.2, which remains close to that expected of AlOOH (2:1) but significantly deviate from that of $Al(OH)_3$ (3:1). These results suggest that the native oxide grown on the aluminum surface is primarily composed of an aluminum oxyhydroxide.

It is important to keep in mind that the possible presence of carbonate species may complicate the accurate estimation of O_{inorg} (see section S1.2, Supplementary material). In this case, a fraction of carbonate species is included in the estimated O_{inorg} molar concentration. This may explain why the $(O_{inorg}/Al^{III})_{corr}$ values for AlOx are slightly higher than the expected stochiometric ratio of AlOOH.

The situation is more evident for the T-AlOx sample. The results show a $(O_{inorg}/Al^{III})_{corr}$ ratio equal to 1.5 ± 0.1, which is remarkably consistent with that expected for the stoichiometry of Al_2O_3. This clearly

Table 1
Chemical composition (elements and decomposition of C 1s, O 1s and Al 2s peaks; mole fraction with respect to the sum of all elements except hydrogen, %). Errors were calculated using the method reported elsewhere [69]. (Abbreviations: E_b = binding energy; bdl. = below detection limit). O_{tot}/Al^{III} and O_{inorg}/Al^{III} ratios obtained from XPS analysis for AlOx and T-AlOx samples prior to (labeled "none") and after immersion in water for 3 h. The ratios were calculated using raw and corrected data with corrections made to account for the differential screening effect due to the presence of adventitious contamination layer.

	C 1s					O 1s	Al 2s			(O_{tot}/Al^{III}) (raw)	(O_{inorg}/Al^{III}) (corrected)
Mean E_b (eV)	[C-(C,H)] 284.8	[C-(O,N)] 286.3	[C=O] 287.7	[O-C=O] 289.2	C_{tot}	531.3	Al^0 116.5	Al^{III} 119.2	Al_{tot}		
AlOx - none	21.1	2.6	1.8	1.6	27.1	42.8	11.4	18.8	30.2	2.3 ± 0.4	2.2 ± 0.2
AlOx – 3h	23.2	2.8	2.1	1.5	29.6	43.3	8.9	18.2	27.1	2.4 ± 0.4	2.3 ± 0.2
T-AlOx - none	14.0	1.7	0.7	1.3	17.7	49.4	bdl.	33.0	33.0	1.5 ± 0.2	1.5 ± 0.1
T-AlOx – 3h	16.0	1.3	0.8	1.5	19.6	48.0	bdl.	32.4	32.4	1.5 ± 0.2	1.5 ± 0.1

indicates that the thermal treatment leads to the growth of stoichiometric alumina on the metallic surface.

The presence of surface hydroxyl groups (−OH) at the outermost layer cannot, however, be reliably probed by XPS; it requires the use of other techniques with higher sensitivity for such chemical groups, particularly when they are organized in a 2D structure, such as ATR-FTIR and SFG.

The ATR-FTIR spectra of AlOx and T-AlOx surfaces are presented in Fig. 2A and B. Both show absorption bands compatible with the formation of oxidized and hydroxylated Al moieties.

First, the 1200-600 cm^{-1} range contains the most intense band, at 943 cm^{-1} for AlOx and 951 cm^{-1} for T-AlOx, which is accompanied by a shoulder in the 750-780 cm^{-1} range. Bands in this range are generally assigned to ν(Al-O-Al) stretching modes [70]. While the positions observed for our samples are higher than those reported for bulk phases of either Al_2O_3, AlOOH or $Al(OH)_3$, the band profiles are quite similar to those observed for Al thin layers deposited on glass and subsequently oxidized by pure O_2 [71]. In the uncalcined sample AlOx, there is another band at 1120-1125 cm^{-1}, most likely due to a δ(Al-O-H) bending mode [71,72]. This position does not correspond to those observed in AlOOH (boehmite), whose structural OH exhibits separate symmetrical and asymmetrical bending modes at 1157 and 1068 cm^{-1} (the latter being the more intense) [73,74], nor to the structural OH of gibbsite Al $(OH)_3$ (914, 966 and 1019 cm^{-1}, most intense) [75]. The single

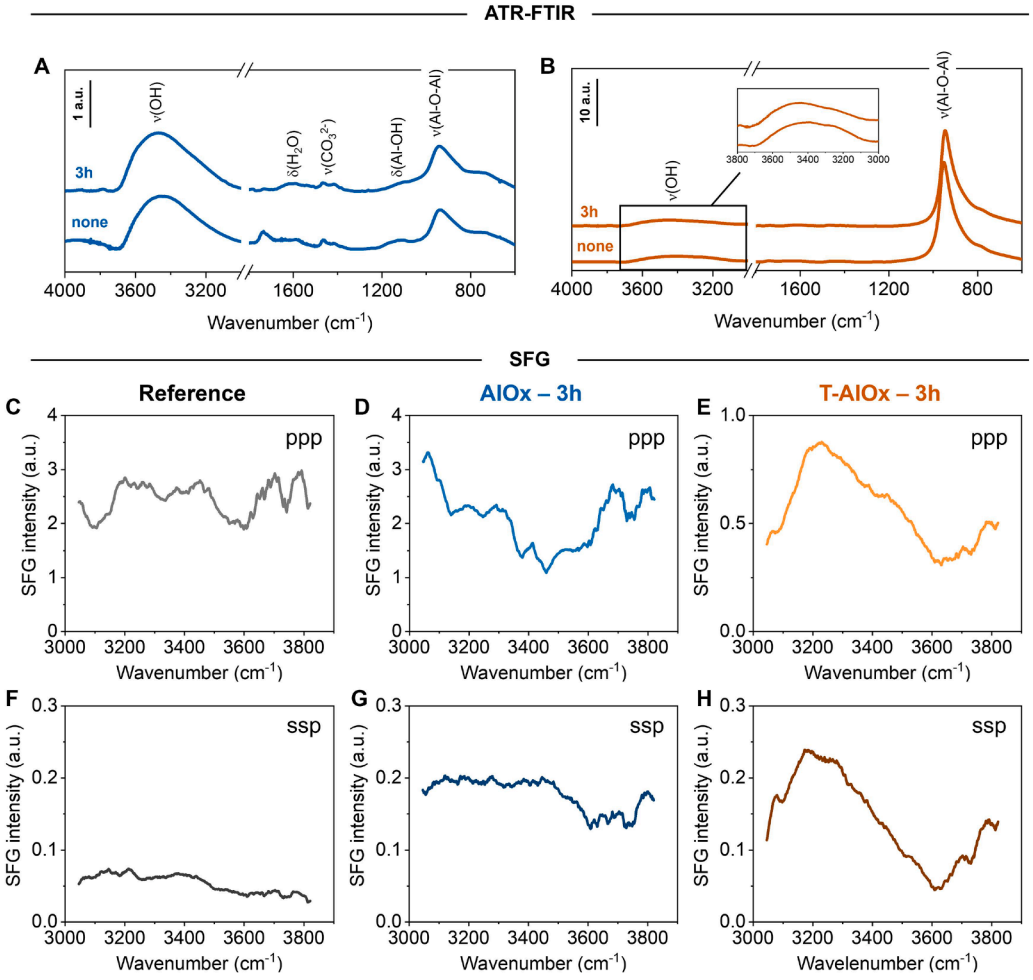

Fig. 2. ATR-FTIR spectra of (A) AlOx and (B) T-AlOx surfaces prior to ("none") and after immersion in water for 3 h. The absorbance scale in the inset of panel 2B is adjusted to be the same as in panel 2A for the sake of comparison. (C-H) Experimental SFG spectra recorded on AlOx and T-AlOx surfaces after immersion in water (3 h) over the 3040–3840 cm^{-1} spectral range in ppp-polarization (C-E) scheme and ssp-polarization (F-H) scheme. The reference used is AlOx surface prior to incubation.

δ(Al-O-H) bending and the high water content (see below) are more reminiscent of strongly hydrated pseudoboehmite, although not identical to it. After calcination to T-AlOx, this band is not discernable anymore; in contrast, the band at 951 cm^{-1} increases by an order of magnitude and becomes dominant in the spectrum.

Second, in the 1900-1200 cm^{-1} range, the bending mode of H_2O is visible at 1623 cm^{-1} for AlOx. It decreases by a factor of 2.5 after calcination. Additional signals at 1415 and 1465 cm^{-1} are probably due to adsorbed (hydrogeno)carbonate species [76,77].

Third, in the 2800-4000 cm^{-1} range, one can observe a very broad signal due to the OH stretching vibrations of both water molecules and Al-OH groups. It is almost featureless, in strong contrast with the well-defined signals observable for bulk AlOOH and $Al(OH)_3$ [73–75], except for the appearance of a shoulder at 3265 cm^{-1} in T-AlOx, and it decreases by a factor of ~2.3 upon calcination.

Finally, in the near IR, the overtones of the OH stretching vibration are found between 6000 and 7800 cm^{-1} and strongly decrease upon calcination (see Fig. S1).

From these observations, we can conclude that an oxidized Al layer exists on both AlOx and T-AlOx systems. It does not consist in any well-defined crystallographic phase, be it an Al hydroxide, an oxyhydroxide or an oxide, although it has some similarities to "pseudoboehmite". However, the relative amount of Al-OH groups is definitely higher on AlOx, and significantly decreases on T-AlOx, while the absolute intensity of Al-O-Al increases by a factor of 10: thus, the thickness of the oxidized layer increases considerably upon calcination, as already observed by XPS, while the surface density of aluminols is much reduced, probably by condensation of aluminol pairs with the emission of water.

The immersion of AlOx and T-AlOx in aqueous medium does not lead to a notable change of the surfaces, at least not in the time scales studied: no significant evolution of the infrared spectra was observed after 3 hours. Also, the decrease in surface Al-OH groups caused by calcination was not reversed by reexposure to liquid water for 3 h.

To obtain detailed insights into the outermost surface composition of both samples before and after immersion, additional sum-frequency generation (SFG) spectroscopy measurements were conducted. As a surface-specific technique, SFG provides vibrational spectra free from bulk contributions and can also give access to molecular orientation information by polarization combination (ppp or ssp) of the SFG, visible and IR beams, respectively. This makes it particularly relevant for probing the structural organization and relative density of hydroxyl groups on aluminum oxide surfaces. The hydroxyl composition of AlOx and T-AlOx was investigated by SFG in the 3000-4000 cm^{-1} spectral range of the OH stretching vibration modes after 3 hours of immersion. Results are presented in Fig. 2C-H. On AlOx surface prior to immersion, used as the reference, only the optical (UV-Visible) contribution to the SFG signal of the aluminum substrate is detected prior to immersion (Figs. 2C and 2F); the observed signal corresponds to the substrate electronic properties (broad interband electronic transition). After immersion in water, a molecular broad band (dip-shaped) appears on AlOx (Fig. 2D), attributable to surface hydroxylation. However, based on the band shape, the amount of OH groups is small. Moreover, these hydroxyl groups appear to be poorly organized, if at all, as confirmed in ssp polarisation (Fig 2G) where no significant contribution and therefore no preferential organization appears in the SFG signal. On T-AlOx, following immersion in water for 3 h, a significant increase in SFG signal intensity is observed, with two distinct and dominant vibrational bands (peak-shaped) appearing at 3230 cm^{-1} and 3475 cm^{-1} in the ppp polarization configuration (Fig. 2E). In the ssp configuration (Fig. 2H), the 3230 cm^{-1} band remains prominent, accompanied by a weaker shoulder at 3475 cm^{-1}. According to the literature, these two bands can be attributed to strongly hydrogen-bonded OH stretching modes of interfacial water arising from ice-like and liquid-like structures of water molecules [78,79]. The increased intensity and distinct shape of these vibrational bands after thermal annealing indicate a higher degree of structural organization at the T-AlOx surface, with a rather rigid and stable structure of the oxide layer indicated by the more intense response of the ice-like contribution to the SFG signal in both polarization schemes with respect to the liquid-like contribution. Besides, the stronger signal in ppp polarization further suggests a preferential vertical orientation of the OH groups because it probes the z-direction normal to the substrate surface.

3.2. Surface topography

The topographical properties of AlOx and T-AlOx surfaces were investigated by means of AFM. Initially, images were acquired in air at various scales on freshly prepared samples (Fig. 3A, B). The typical images obtained did not reveal any significant differences between the AlOx and T-AlOx surfaces: polishing-induced striations are clearly visible, along with a few isolated particles dispersed across the surfaces. Height variations appear to be slightly more pronounced on the T-AlOx surface, as shown by the scan lines (Fig. 3A, B). This description, however, remains qualitative and does not allow for a clear assessment of the effect of thermal treatment on the surface topographical properties.

Actually, these surfaces, like many other metal oxides, typically display random topographies that can be characterized using a fractal formalism [80]. In a conventional three-dimensional coordinate system, where the (x,y) plane represents the average surface plane, fluctuations perpendicular to this plane can be described by a statistical variable known as the height function $h(x,y)$. The surface roughness is considered self-affine if it remains invariant under anisotropic affine transformations of the following form:

$$\begin{matrix}(x,y)\rightarrow(\lambda x,\lambda y),\\ h(x,y)\approx\lambda^{\zeta}h(\lambda x,\lambda y)\end{matrix}\quad \text{for } x,y\neq 0 \tag{11}$$

where λ is the scaling factor and ζ is the roughness exponent, which is considered as a quantification of the roughness changes with the length scale.

The roughness measurement depends on the length scale over which it is performed. A common measure of roughness at a given length scale L is the root-mean-square roughness of the height differences across a two-dimensional surface of area L^2:

$$w(L)=\left(\frac{1}{L^2}\int_0^L\int_0^L[h(x,y)-\overline{h}]^2dxdy\right)^{\frac{1}{2}} \tag{12}$$

where the mean height is given by $\overline{h}=\frac{1}{L^2}\int_0^L\int_0^L h(x,y)dx\,dy$. For self-affine surfaces obeying Eq. (11), the root-mean-square of the height differences is expected to scale as:

$$w(L)\approx L^{\zeta} \tag{13}$$

The log-log $w(L)$ versus L plots are presented in Fig. 3C and D. They demonstrate that the root-mean-square roughness follows a power law at small length scales for both AlOx and T-AlOx surfaces, as predicted by Eq. (13). At larger scales L, the roughness w saturates, suggesting the presence of a lateral cutoff length L_c, beyond which $w(L)\approx w_{sat}$ (when $L\gg L_c$). This cutoff length, also referred to as the crossover length, marks the scale below which surface height fluctuations remain laterally correlated.

Accordingly, both AlOx and T-AlOx can be considered as self-affine surfaces, which obey the anisotropic scale invariance (Eq. 11), and may be characterized by three parameters [81]: (i) the saturation value of the roughness, w_{sat}, which is an amplitude (vertical) parameter, (ii) the roughness exponent ζ, which is related to the jaggedness of the surface, and (iii) the crossover length, L_c, which is a lateral spatial parameter. These three parameters derived from *w(L) vs L* plots are given in Table 2 for both AlOx and T-AlOx.

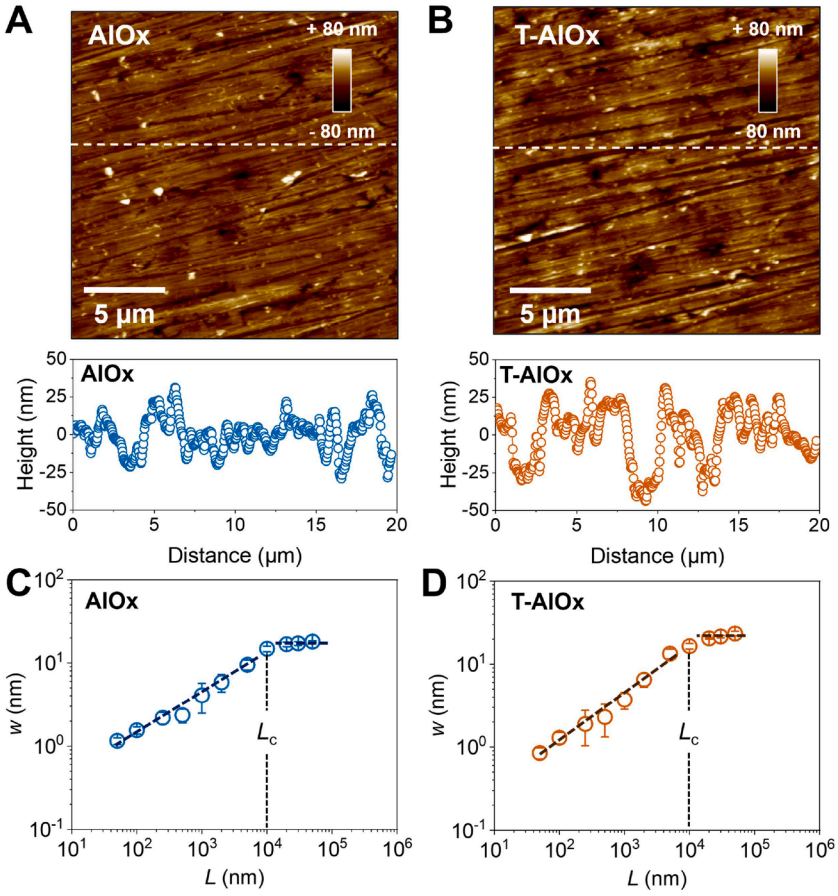

Fig. 3. AFM height images (20 µm x 20 µm) recorded in air on (A) AlOx and (B) T-AlOx and their corresponding scan lines measured at the location indicated by the dotted line. (C, D) log-log plots showing the evolution of the root-mean-square roughness, $w(L)$, as a function of the length scale, L. The error bars are standard deviations from scans recorded at different locations on the sample surface. Dashed lines indicate the roughness changes predicted by Eq. (13) for $L < L_c$ and the saturation at large length scales, i.e. $L > L_c$.

Table 2
Roughness parameters derived from *w(L) vs L* plots presented in Fig. 3C and D.

	w_{sat} (nm)	ζ	L_c (nm)
AlOx	17.0	0.48 ± 0.02	9860
T-AlOx	21.9	0.57 ± 0.02	9860

The saturation value of the roughness w_{sat} is affected by the thermal annealing process; it increases slightly from 17.0 for AlOx to 21.9 nm for T-AlOx (Table 2). The values of the lateral cutoff length L_c remain identical, indicating that the topographies of the two surfaces exhibit a similar degree of randomness. L_c defines, indeed, the upper limit of the lateral scale over which the surface roughness exhibits self-affine behavior. It essentially represents the maximum correlation length beyond which height fluctuations become uncorrelated. A similar L_c values for both samples means that the spatial extent of surface correlations remains unchanged by the thermal treatment. Furthermore, although there is a significant variation, the roughness exponent remains close to 0.5 (Table 2). This parameter characterizes how the surface roughness scales with lateral distance in the self-affine regime. A value around 0.5 is often associated with random-walk-like or uncorrelated growth; the two similar values for AlOx and T-AlOx imply that the surfaces have similar scaling behavior and that the underlying physical mechanisms governing surface topography have not been significantly altered by the annealing. This supports a growth mechanism predominantly occurring at the metal/oxide interface rather than on the outermost part of the oxide.

Subsequently, AlOx et T-AlOx surfaces were imaged in aqueous solution, i.e., under the same conditions as the peptide interaction measurements are carried out, to investigate any potential evolution of the topography as a function of the immersion time. AFM height images of AlOx and T-AlOx recorded in water after various immersion times ranging from 45 minutes to 3 hours are presented in Fig. 4A and 4B, respectively. When immersed, homogeneously distributed nanostructures with a size of a few nanometers appear almost immediately on both surfaces, fewer in number for T-AlOx. They can be observed on the scan lines in Fig. 4C and 4D for AlOx and T-AlOx, respectively. The height of the observed nanostructures was measured at every immersion time from scan lines and pooled into height histograms as their size did not vary with the immersion time. They are presented for AlOx and T-AlOx in Fig. 4E and 4F, respectively. The difference between the two surfaces is around 1 nm, with a mean height of 8.6 ± 0.1 nm for AlOx, and 7.0 ± 0.1 nm for T-AlOx, which is relatively small for this type of surface. The average roughness at this scale (Fig. 3C, D) is similar for T-AlOx (R_{rms} = 6.5 ± 1.2 nm) as for AlOx (R_{rms} = 5.9 ± 1.4 nm) and no evolution of the surfaces is observed during immersion.

3.3. *Surface hydrophobicity*

Nanoscale surface hydrophobicity was probed in water using a gold-coated AFM tip functionalized with alkane thiols exhibiting non-polar $-CH_3$ end groups as depicted in Fig. 5A. Typical F-D curves obtained as the functionalized tip was retracted from AlOx and T-AlOx surfaces are given in Fig. 5B. Some F-D curves exhibit adhesion events, all observed at nearly zero distance (Fig. 5B, labels b-d), while others do not

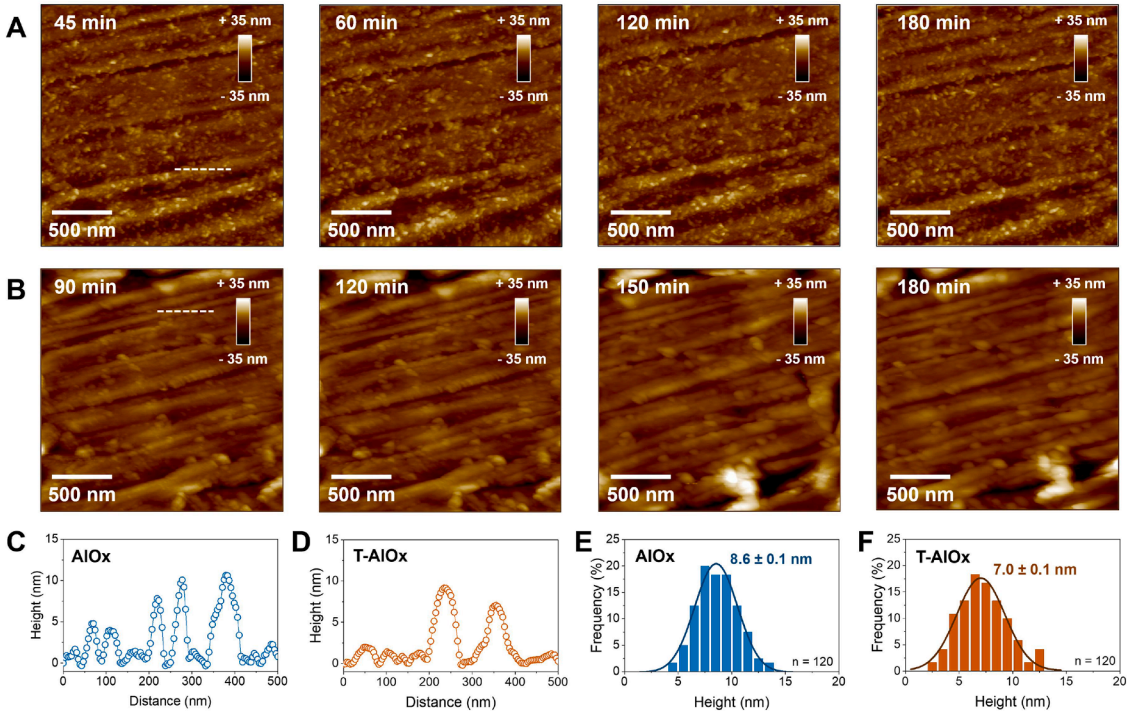

Fig. 4. AFM Height images (2 × 2 μm^2) recorded in water of (A) AlOx and (B) T-AlOx at various immersion time. (C, D) scan lines were taken at the locations indicated by dashed lines in the height images (A,B), respectively. Height histograms of the rod-shaped structures observed on (E) AlOx and (F) T-AlOx (n = 120 for both surfaces). Data of the height histograms were pooled from all immersion time images recorded.

(Fig. 5B, label a). These adhesion events reflect the existence of hydrophobic forces due to the interaction between the hydrophobic probe and a "hydrophobic" area present on the oxide surface, as illustrated in Fig. 5A.

Adhesion forces probed on AlOx and T-AlOx surfaces were plotted into a force histogram presented in Fig. 5C and D. They show a non-adhesion frequency of about 94% on AlOx (Fig. 5C), which is significantly higher than that of T-AlOx (47%, Fig. 5D). In the latter case, adhesion forces are mostly gathered in the 50-400 pN range. To obtain information on the spatial distribution of the hydrophobic areas probed, hydrophobicity maps were created by attributing each adhesion force to a pixel on a map of the surface. A rough estimate of the probed area at each pixel can be made using the JKR model (see section S3, Supplementary material), yielding a value equal to 7.6 nm^2.

The hydrophobicity map obtained on the AlOx surface (Fig. 5E) reveals that a large majority of the surface probed does not exhibit any adhesion events (about 95%). The remaining 5% is gathered in only a few isolated events and in specific areas (dark red blotches on the adhesion map), with forces ranging from 100 pN to 600 pN, sometimes exceeding 1 nN. The situation on T-AlOx (Fig. 5F) is very different. The adhesion events (about 53%) are randomly distributed along the surface plane and cover almost the entire surface. These results suggest the existence of hydrophobic areas on the T-AlOx surface, whereas they are hardly detected on the AlOx surface.

What is the nature of these hydrophobic areas? It may initially be assumed that these regions arise from adventitious contamination, which results in the adsorption of organic compounds, mainly of hydrocarbon nature, on these high surface energy solids. However, XPS analysis revealed that the carbon content on the T-AlOx surface, where hydrophobic areas were clearly observed, is significantly lower compared to AlOx (Table 1). This behavior is consistent with the presence of adsorbed water molecules, as confirmed by IR and SFG data, which compete with the adsorption of organic contaminants. Accordingly, the hydrophobic interactions measured on the T-AlOx surface appear to be associated with intrinsic Al–O–Al sites rather than with adventitious organic contaminants.

3.4. Surface charge

Colloidal probe force spectroscopy offers an outstanding way to locally probe the surface charge by measuring the variation of the force as the colloidal probe enters the EDL formed at the surface-liquid interface. As schematized in Fig. 6A, the probe is approached towards the surface and is subjected to either attractive or repulsive interaction, depending on the local surface charge. This method has been used to provide an estimate of the isoelectric point (IEP) of aluminum oxide surfaces, defined as the pH at which the surface exhibits a net neutral charge, by performing measurements at various pH and detecting the switch from attractive to repulsive interactions at the IEP [64,82,83].

In this study, a silicon oxide colloidal probe, exhibiting negatively charged silanol groups at the studied pH (6.8 ± 0.1), was used. The ionic strength, and thus the thickness of the EDL, was set by adding an indifferent electrolyte in the medium (KNO_3 10^{-5} M). Typical approach F-D curves obtained during the measurements for AlOx (circle, blue) and T-AlOx (square, orange) are presented in Fig. 6B. On AlOx, F-D curves show an increase of the force, starting at a distance to the surface of about 150 nm, and suggesting a probe-surface repulsion, changing to an attraction closer to the surface, at a distance of about 15 nm. By contrast, on T-AlOx, F-D curves did not show a significant increase of the force upon approaching the probe to the surface, but they did show the attractive behavior at close distances. Only weak variations can be observed at different locations where the F-D curves are recorded (see Fig. S3).

The F-D curve profiles can be interpreted on the basis of the DLVO model (see section 2.7). At large separation, the variation of the force is almost entirely due to long-range electrostatic interactions. As the probe comes closer to the surface, short-range van der Waals attraction will dominate the interaction, leading to a "jump-to-contact" of the tip to the surface. However, these observations are only qualitative. To provide reasonable estimates of the interactions probed, the extracted F-D curves

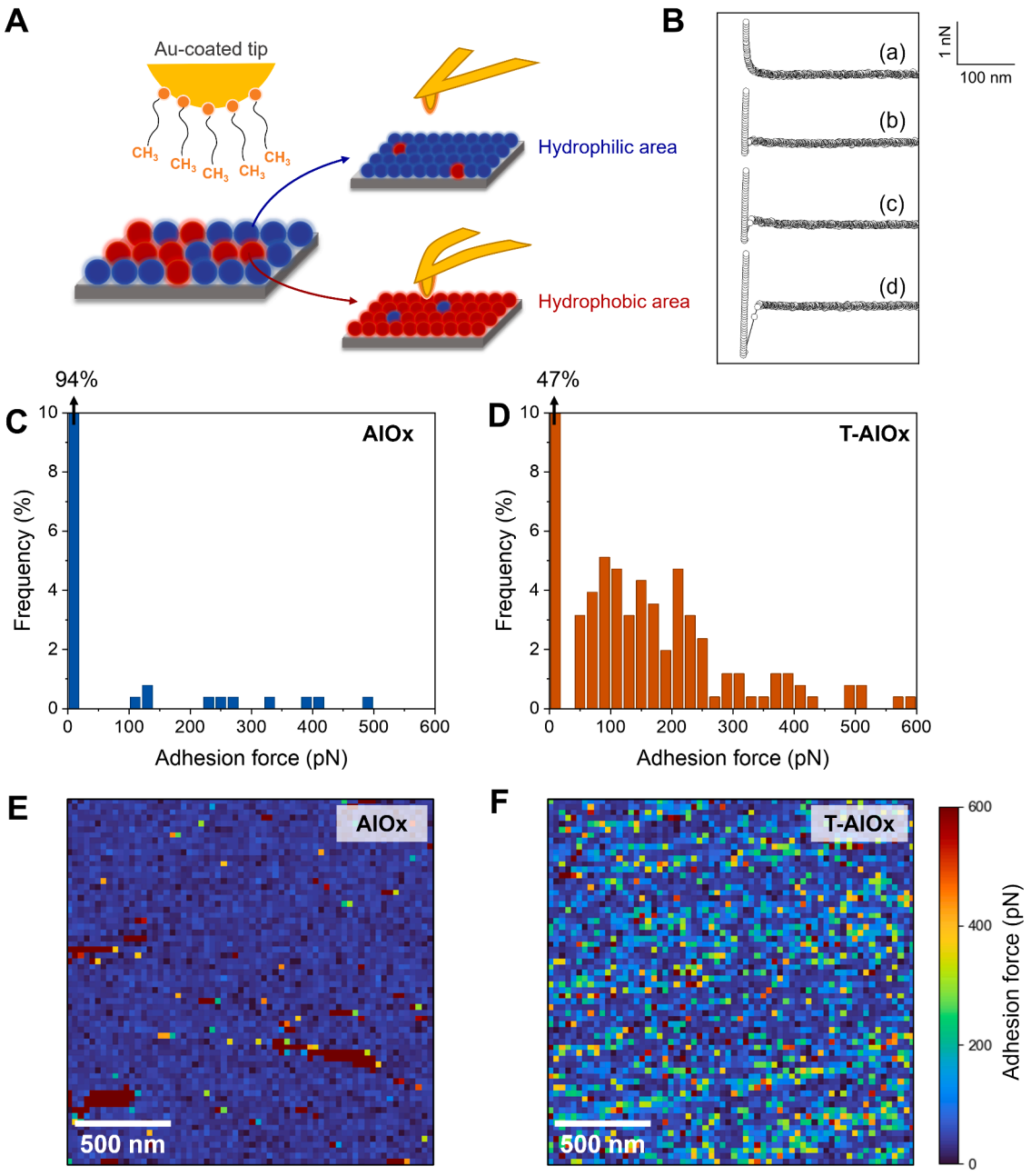

Fig. 5. (A) Scheme depicting surface hydrophobicity measurements using a (–CH_3)-functionalized gold-coated AFM tip in water. (B) Typical retract F-D curves recorded on AlOx and T-AlOx. Force histograms obtained from measurements performed on (C) AlOx (n = 4096) and (D) T-AlOx (n = 4096) and their corresponding hydrophobicity map (2 × 2 μm^2), (E) and (F), respectively, where each pixel corresponds to an adhesion force value extracted from the corresponding force curve.

can be fitted with the DLVO model. For each fitted curve, a value of the surface potential (ψ_{Surf}) can be extracted (Eq. (1)). All ψ_{Surf} values from F-D curves collected on AlOx or T-AlOx surfaces were then plotted in histograms, which are presented in Fig. 6E. The mean values of ψ_{Surf} obtained from gaussian fits were -21.56 ± 0.24 mV and +12.99 ± 0.17 mV for AlOx and T-AlOx, respectively. These results show that the AlOx surface is overall negatively charged, in agreement with the IEP values reported for many planar aluminum oxide surfaces, including alumina, which are in the range of pH 4.0 to 6.5 [64,78,84–88].

The situation is more complex for T-AlOx surface. First, most of the F-D curves obtained do not exhibit any profile that can be easily attributed to attractive or repulsive interactions: the net force in this distance range is close to zero (Fig. 6D). Second, the ψ_{Surf} distribution, while being centered around a positive value, spans a range of values from -20 mV to over +40 mV (see Fig. 6E). Third, the positive value of ψ_{Surf} at pH 6.8 ± 0.1 suggests an IEP value greater than pH 7.0. This latter result is in agreement with values measured on dispersed Al_2O_3 particles by potentiometric methods (8.0 to 10.0 range), but it clearly deviates from the trend observed in the literature for the basal plane of sapphire/corundum [64,78,84–88]. This result is expected for native oxide surfaces, where the presence of multiple crystalline phases with diverse orientations, as well as edges and defects make them chemically closer to powders rather than model substrates. To confirm this, we also performed colloidal probe experiments on a model, single-crystal, alumina surface (C-Al_2O_3 (0001)) in the same conditions as for T-AlOx surfaces. On C-Al_2O_3 (0001), we found a negative ψ_{Surf} at -19.42 ± 0.04 mV (compare Fig. S4A and B), indicating an IEP < 7 in agreement with results found in the literature.

This validates colloidal probe measurements and experimental modeling data. T-AlOx surface differs from C-Al_2O_3 by the fact that it is

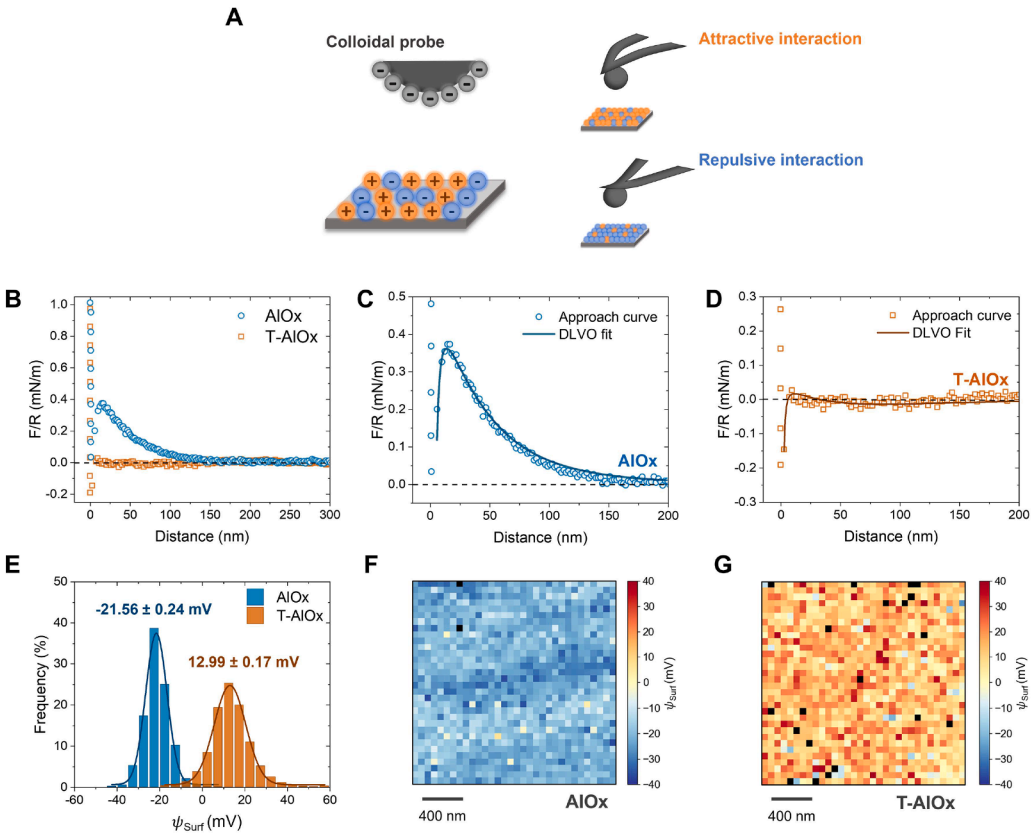

Fig. 6. (A) Scheme depicting colloidal probe measurements used to study the surface charge of AlOx and T-AlOx surfaces in a KNO_3 10^{-5} M solution (pH 6.8 ± 0.1). (B) Approach F-D curves plotted against the separation distance between the colloidal probe and the AlOx (○, blue) and T-AlOx (□, orange) surfaces. F-D approach curves recorded on (C) AlOx and (D) T-AlOx with DLVO model fitting. (E) Distribution of the surface potential (ψ_{Surf}) values obtained from the fitting for AlOx and ψ_{Surf} map of (F) AlOx (n = 1022) and (G) T-AlOx (n = 1004 F-D curves) surfaces, where for each pixel a ψ_{Surf} value was extracted from a F-D curve fitted with the DLVO model. Black pixels correspond to F-D curves that cannot be exploited.

composed of a superficial oxide layer formed on a polycrystalline metallic aluminum substrate. Therefore, even if the stoichiometry is comparable to that of alumina crystals such as sapphire, T-AlOx probably also exhibits several different crystal planes with different molecular environments of the charge-determining surface groups. This is borne out by the fact that the width of the electric potential distribution on T-AlOx is larger than on C-Al_2O_3 (0001) (FWHM of about 9 mV against 4 mV). Now while the (0001) plane of the corundum structure exhibits OH groups coordinated to 3 Al^{3+} (μ^3) which are highly acidic and therefore deprotonated at even low pH, other planes contain bridging (μ^2) and terminal OH groups that are less acidic – and more basic, accounting for the higher IEP [89].

The change in the IEP may have another origin. Dissolution at the oxide/water interface leads to the continuous release of Al^{3+} and OH^- ions, which impacts the composition and the organization of the EDL (and may finally result in reprecipitation as $Al(OH)_3$, possibly explaining the nanostructures seen by AFM). To explore this effect, surface charge measurements were performed in the same conditions on C-Al_2O_3 surface, while adding Al^{3+} ions in the medium. The ψ_{Surf} value shifts from a mean value of -19.42 ± 0.04 to +3.87 ± 0.05 mV in the presence of Al^{3+} ions (see Figure S4D, Supplementary material). These results suggest that the ψ_{Surf} of aluminum oxides probed by colloidal probe can, indeed, be influenced by the release of Al^{3+} ions in the aqueous medium: they could adsorb in the Stern layer, making the surface more positive at a given pH. A similar effect was observed on kaolinite using zeta-potential measurements after adding aluminum ions in the solution [90]. However, data obtained on alumina nanoparticles show that while dissolution/reprecipitation phenomena may indeed occur at pH close to neutrality, they have a slow kinetics and may take several tens of hours at room temperature [91]. In the present study, the presence of Al^{3+} ions at the solid/liquid interface is difficult to probe accurately on planar surfaces and the question would deserve further investigations.

The wide distribution of charge observed on AlOx and T-AlOx surfaces raises questions about spatial heterogeneity of the surface sites. To investigate this heterogeneity, ψ_{Surf} maps were created by attributing each approach force curve fitted with the DLVO model to a pixel on a map of the surface. The probed area at each pixel is estimated to be around 50 nm^2 (see section S3, Supplementary material). The ψ_{Surf} maps of AlOx and T-AlOx are presented in Fig. 6F and 6G, respectively. The AlOx map only reveals a mild heterogeneity of the sites probed on the surface. In contrast, T-AlOx map shows a higher heterogeneity of the sites, that could be related to the existence of surface sites with different reactivities, on different crystal planes or not, or to the adsorption of the Al^{3+} ions released from the dynamic state of the metal/oxide/solution interface. This will most probably have an impact on the molecular interactions formed with the peptide.

3.5. *Single-molecule force spectroscopy (SMFS)*

Results from chemical and topographical characterizations revealed that AlOx and T-AlOx surfaces exhibit an aluminum oxide layer formed on top of the metallic substrate. A higher degree of structural organization of the oxide layer was found on T-AlOx following the thermal annealing process (SFG data), as well as a stoichiometry closer to Al_2O_3 (XPS data). In addition, a significant difference is found at the local scale between AlOx and T-AlOx surfaces, regarding both surface charge and local hydrophobicity. SMFS was used to explore the impact of these differences on the interaction with a dipeptide Glu-Ala.

The tip functionalization procedure used in this study was originally developed by Gruber et al. for biological receptors using an acetal-PEG-NHS linker [55]. This procedure was further explored to probe the interaction between oligopeptides and metallic surfaces [39,48]. It provides a configuration where the fragment of the Glu-Ala peptide of interest is exposed for interaction with the surface, while involving the [–NH_2] group in the coupling with the linker through a Schiff base (Fig. 7A). Specifically, here, two carboxylic acid functions [–COOH] from the C-terminus and the lateral chain of Glutamic acid, as well as the amide function [–(CO)–NH] of the peptidic bond and the [–CH_3] of the Alanine are expected to be accessible to the aluminum surface.

Fig. 7B presents typical F-D curves obtained when recording approach-retract cycles of a peptide-modified tip with the aluminum oxide surface at a constant loading rate (r), only retract curves being shown and explored. As described in a previous study [48], this type of experiment yields a large panel of F-D curves due to the abundance of the surface sites that are accessible to interact with the functional groups of the biomolecule that is immobilized on the tip. In the present study, while showing great variation, F-D curves can still be roughly classified into 3 types: (i) curves not showing any adhesion event (Fig. 7B, label a), (ii) curves exhibiting only one adhesion event, either characterized by a PEG elongation before the rupture of the interaction a few nanometers away from the surface (Fig. 7B, label b), or not, i.e. occurring at nearly zero distance (Fig. 7B, label c), and (iii) curves displaying multiple adhesion events (Fig. 7B, label d). F-D curves exhibiting a PEG linker unfolding were analyzed using the worm-like-chain (WLC) model, yielding a contour length ranging from 2.5 to 7.9 nm (see Fig. 7B). These values fall within the range expected for the PEG linker used in this study (M_w = 1241.4 g.mol^{-1}) [92], but also indicate that the linker does not undergo a complete unfolding in each peptide-surface interaction. This is a major issue, as linker unfolding is usually a valuable parameter for sorting the single events of interest and avoid “non-specific” interactions, mainly involving tip-surface and PEG-surface interactions. Working on heterogeneous oxide surfaces is therefore a challenge, as the adhesion forces can be sometimes too weak to be systematically preceded by linker unfolding. Control experiments using either a bare AFM tip or one functionalized only with PEG (without the peptide) revealed a proportion of non-adhesive events exceeding 90% (Fig. 7D, F). This suggests that the peptide-surface interaction dominates, whereas the PEG linker has a negligible contribution in the force histograms. Indeed, when all the adhesion forces probed between the peptide fragment and the aluminum oxide surfaces are pooled, meaningful adhesion events are observed for both AlOx and T-AlOx surfaces (Fig 7C and E). On AlOx, the non-adhesion events showed a frequency of 46%, and a gaussian fit of the force histogram yields a most probable force of adhesion, F^*_{adh}, equal to 152.8 ± 4.0 pN. On T-AlOx, the non-adhesion frequency decreased markedly to 15%, while the F^*_{adh} value remained almost unchanged, of 158.5 ± 4.0 pN.

The adhesion events collected on a 2 × 2 μm^2 area are presented in force maps in Fig. 7G and 7H for AlOx and T-AlOx, respectively. On these maps, each pixel corresponds to one adhesion force value, extracted from the corresponding F-D curve. The maps explicitly show that more adhesion events are probed on T-AlOx surface compared to AlOx. Moreover, these adhesion events are not localized in a specific area but rather randomly distributed across the whole probed surface.

These results provide a valuable basis for comparing the two surfaces in terms of interaction with the peptide, revealing that although the adhesion forces are of similar magnitude, adhesion events occur more frequently on T-AlOx than on AlOx. However, this observation is not sufficient to quantify the interaction. For this purpose, dynamic force spectroscopy measurements were performed and the dependence of the most probable adhesion force, F^*_{adh}, to the logarithm of the loading rate, r, was plotted for both the AlOx and T-AlOx surfaces (Fig. 7I and J). The F^*_{adh} vs log(r) plots show relatively different profiles between AlOx and T-AlOx. However, in both cases, two behaviors are observed that can correspond to the regimes predicted by the Friddle-Noy-De Yoreo (FNDY) model. At low loading rates ($r < 5.10^5$ pN.s^{-1} for AlOx and $r < 1.10^5$ pN.s^{-1} for T-AlOx), only weak variations of the F^*_{adh} are observed, yielding a plateau at about 78 pN for AlOx (Fig. 7I), and 73 pN for T-AlOx (Fig. 7J). In the high loading rates region ($r > 10^6$ pN.s^{-1}), the force required for bond rupture increases linearly with increasing the logarithm of the loading rate. The latter regime is consistent with the prediction of the Bell-Evans (BE) theory.

By applying the BE model, the width of the energy barrier (x_t) was extracted from the slope of the linear fit (see Eq. (2)) and the kinetic off-rate (k_{off}) was obtained from the intersection of the linear fit with the x-axis (see Eq. (3)). This yields values of x_t = 0.46 Å and k_{off} = 4973.2 s^{-1} for AlOx and x_t = 1.11 Å and k_{off} = 387.8 s^{-1} for T-AlOx, which are consistent with the values obtained from the FNDY model (x_t = 0.39 Å and k_{off} = 4209.6 s^{-1} for AlOx and x_t = 0.99 Å and k_{off} = 376.3 s^{-1} for T-AlOx, see Eq. (7)).

Another important advantage of the dynamic force spectroscopy experiments lies in the possibility to estimate the free enthalpy for adsorption, $\Delta_{ads}G^\circ$, by using the FNDY model when the system is considered at a near-equilibrium regime (see Eq. (8)). This yields values of $\Delta_{ads}G^\circ$ equal to -7.14 ± 0.18 k_BT for AlOx and -9.03 ± 0.57 k_BT for T-AlOx.

An alternative method to extract $\Delta_{ads}G^\circ$ from non-equilibrium single-molecule measurements is based on the Jarzynski equality. This equality explores the fluctuations of the adhesion work measured during the binding-unbinding process using Eq. (10). For the systems studied here, the adhesion work was measured from F-D curves as the integral of the adhesion events as illustrated in Fig. 8A. Works of adhesion obtained for measurements performed on AlOx and T-AlOx with the Glu-Ala peptide were then plotted into work histograms presented in Fig. 8B and 8C, respectively. A gamma fitting of the distributions obtained was used to extract the $\Delta_{ads}G^\circ$. As shown in Fig. 8B and C, the estimated density curve under the Gamma distribution fits very well with the histogram and even with the density estimation obtained without assuming an underlying family. Moreover, we performed a Kolmogorov–Smirnov goodness-of-fit test for the Gamma model, obtaining a p-value of 0.2061 for AlOx and 0.4359 for T-AlOx, which supports the hypothesis that the assumed Gamma model is appropriate. Results of the fittings are given in Table 3. Values of $\Delta_{ads}G^\circ$ are found at -7.42 ± 0.50 k_BT for AlOx and -8.61 ± 0.57 k_BT for T-AlOx, corresponding to -18.38 and -21.33 kJ.mol^{-1}, respectively. It is remarkable that these values agree within 4 to 5% with those found using the FNDY model (Table 3). Although the values obtained for the AlOx and T-AlOx surfaces appear relatively close, a statistical test was performed to assess the relevance of the difference. The analysis yielded a p-value below 0.0001, confirming that the two surfaces behave distinctly. This outcome indicates that the peptide fragment interacts with AlOx and T-AlOx through different mechanisms.

4. Discussion

Two types of planar aluminum (hydr)oxide surfaces, AlOx and T-AlOx (Fig. 1A), have been synthesized and submitted to a combination of characterization techniques, proving a comprehensive description of both surfaces at the macro- and nanoscale levels.

AlOx, produced by room-temperature oxidation of a polycrystalline Al wafer prepared by polishing a pure Al substrate, exhibits a thin native oxide layer, as demonstrated by XPS, which in addition to oxidized species (Al^{III}) still shows an important contribution of the underlying metallic aluminum substrate (Al^0). The ATR-FTIR spectrum, and the XPS O/Al^{III} ratio of about 2.2, suggests that this surface may be similar to pseudo-boehmite, an ill-crystallized precursor of the oxyhydroxide boehmite (AlOOH).

In T-AlOx, obtained by thermal annealing (calcination) at 550°C of the polycrystalline Al wafer, a thicker oxide layer is formed since the Al^0 contribution is no longer observable by XPS (Fig. 1C). This conclusion is

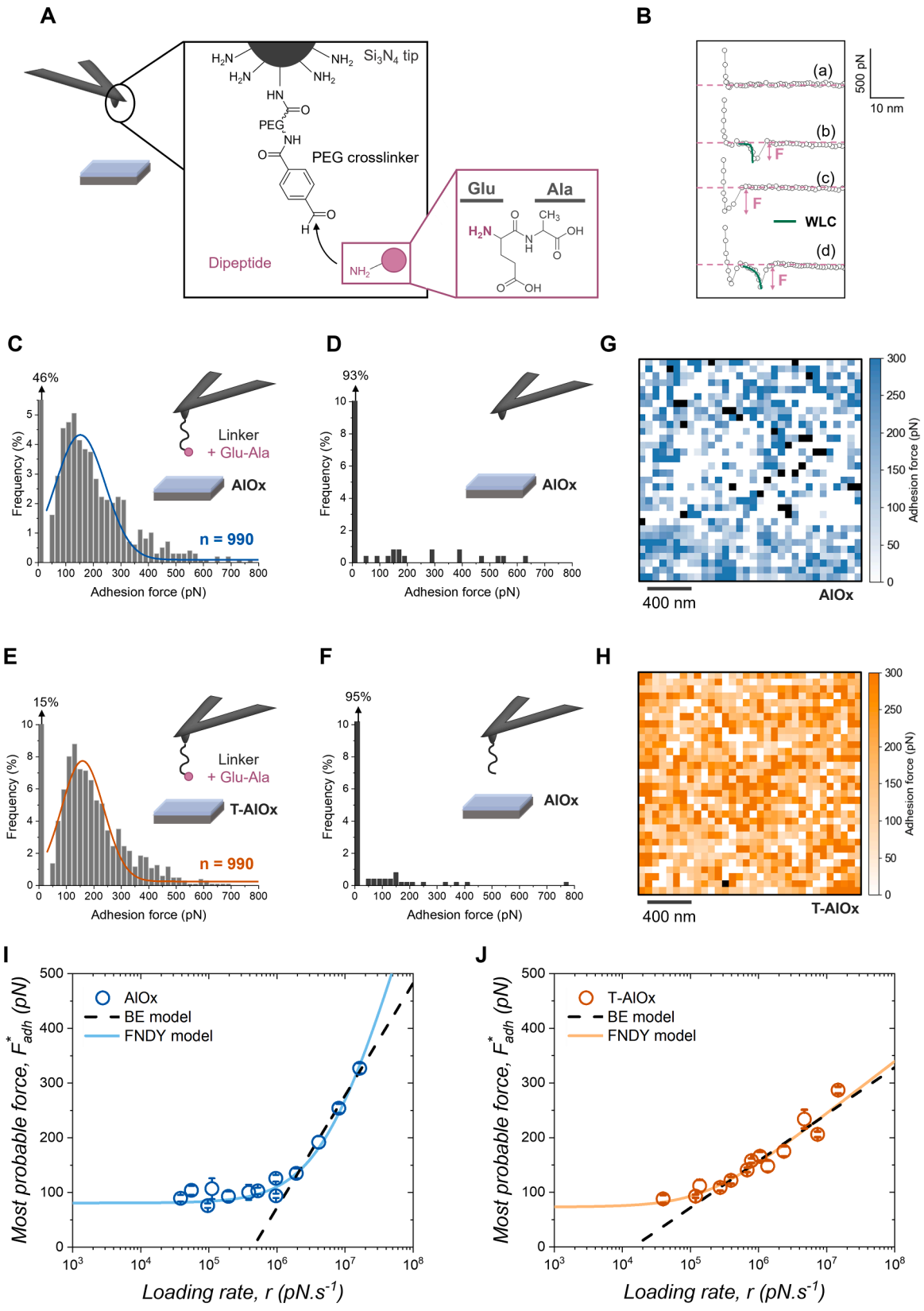

Fig. 7. (A) Scheme depicting the tip functionalization with the Glu-Ala dipeptide. (B) Typical F-D curves recorded by force spectroscopy measurements between the dipeptide-modified tip and the surface. Curves exhibiting a PEG-linker extension were fitted with the worm-like-chain (WLC) model. Force histograms of (C) AlOx and (E) T-AlOx fitted with Gaussian function. Control experiments performed on AlOx surface with either (D) bare AFM tip or (F) AFM tip functionalized with the PEG linker alone. Corresponding force maps of the force histograms for (G) AlOx and (H) T-AlOx surface. (I), (J) The most probable adhesion force F^*_{adh} obtained from the Gaussian fit of force histograms, plotted as a function of the loading rate r and using BE and FNDY model fits, as indicated.

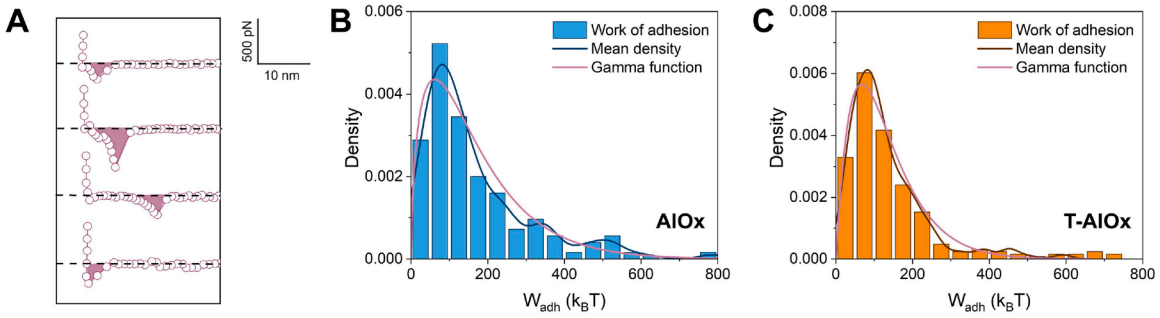

Fig. 8. (A) Example of F-D curves used to extract the work of adhesion W_{adh} from the filled area of the adhesion event obtained from experiments probing Glu-Ala-surface interactions. Work of adhesion histograms obtained for (B) AlOx and (C) T-AlOx surfaces, with the corresponding mean density, as well as curves obtained from a Gamma function fitting of the histograms (n = 249 for each surface).

Table 3
Kinetic and thermodynamic parameters describing for the interaction of Glu-Ala peptide fragment with AlOx and T-AlOx surfaces. Abbreviations. BE=Bell-Evans; JE=Jarzynski equality; FNDY=Friddle-Noy-De Yoreo.

	Unbinding rate constant k_{off} (s^{-1})		Free enthalpy of adsorption $\Delta_{ads}G^{\circ}$(k_BT)	
	BE	FNDY	JE	FNDY
AlOx	4973.2	4209.6	-7.42 ± 0.50	-7.14 ± 0.18
T-AlOx	387.8	376.3	-8.61 ± 0.57	-9.03 ± 0.57

supported by a marked increase of the ν(Al–O–Al) band intensity observed by ATR-FTIR (Fig. 2B). SFG reveals distinct ice-like and liquid-like water bands (Fig. 2E, H), indicating a higher degree of structural organization at the T-AlOx/water interface, which corresponds to a more rigid and stable oxide structure. IR and the XPS O/Al^{III} ratio equal to 1.5 suggest that this surface is similar to that of alumina, Al_2O_3, but remains polycrystalline due to the nature of the underlying metal. This chemical transformation of AlOx (presumably pseudo-boehmite) into T-AlOx (alumina) at 550°C is consistent with reported transition temperature of boehmite to alumina in the literature [77]. Note that both Al_2O_3 (corundum) and boehmite are considered as likely materials of prebiotic relevance by geologists [93].

Despite the growth of the aluminum oxide layer through thermal annealing, no significant changes in surface topography were observed between AlOx and T-AlOx by AFM imaging (Fig. 3). Thus, during thermal annealing, the oxide layer most likely grows at the interface between the metallic substrate and the oxide via interdiffusion of aluminum and oxygen, without altering the outermost surface.

Both surfaces are very reactive towards adsorption immediately after preparation: XPS reveals that they are covered by adventitious organic contaminants. In contrast, upon immersion in aqueous solution for three hours, further adsorption of organic molecules does not seem to occur and no significant changes in the chemical composition of the AlOx nor of the T-AlOx surfaces were detected, nor of their vibrational spectra. However, AFM imaging revealed the formation of small nanostructures, a few nanometers in height, on both surfaces (Fig. 4), which may be due to dissolution/reprecipitation phenomena.

A key question is how local surface characteristics can influence the interaction with individual biomolecules. Notably, local measurements of surface charge (colloidal probe) and hydrophobicity (chemical force microscopy) revealed clear differences between the two surfaces.

AlOx was negatively charged at pH ~ 7, indicating that its IEP is < 7, and showed no evidence of distinct hydrophobic domains. This finding is consistent with SFG data, which suggests that although the outermost surface is hydroxylated, the hydroxyl groups are not disposed with spatial periodicity and cannot impose solvent organization. In contrast, T-AlOx is globally positively charged under the same conditions (IEP > 7, in agreement with literature results for polycrystalline Al_2O_3), but the measured surface potential fluctuates around values close to zero. Moreover, well-defined hydrophobic regions were clearly observed on T-AlOx surface, likely corresponding to Al–O–Al bonds whose formation is promoted by thermal annealing [94,95]. These results suggest that the T-AlOx surface is also hydroxylated, as the AlOx one, but exhibits a more ordered spatial distribution of Al–OH and Al–O–Al groups across the surface, which imposes organization on the interfacial water molecules. Specifically, the detection of hydrophobic forces by chemical force microscopy, randomly distributed over the T-AlOx surface, indicates the presence of (possibly small) regions where Al−O−Al groups predominate, thereby governing local hydrophobicity.

Single-molecule force spectroscopy offers insights into how these local surface properties influence the interaction with a single dipeptide, that would be difficult to obtain with conventional ensemble-averaging techniques. At first sight, in the case of the dipeptide Glu-Ala, dynamic force profiles for interactions with AlOx and T-AlOx are similar. However, closer inspection reveals important differences. First, a significantly higher absolute value of the free enthalpy of adsorption is observed for the peptide-T-AlOx interaction compared to AlOx, in other words the Glu-Ala peptide has a stronger affinity for the T-AlOx surface. While the difference may appear small (an increase of 16 to 26%), it is confirmed by using two different approaches to exploit data on adhesion events (FNDY model and Jarzynski equality).

But beyond adsorption thermodynamics, force spectroscopy also provides information on the kinetic aspects of this phenomenon. Indeed, the dissociation rate constant (k_{off}), which determines the lifetime of the peptide-surface interaction, is significantly higher for AlOx than for T-AlOx, by more than an order of magnitude. Translated into macroscopic terms, this would mean that peptides adsorbed on T-AlOx are not only (somewhat) more stable than on AlOx, but they are significantly more inert, i.e., the desorption process would be slower from T-AlOx.

Both the thermodynamics and kinetics of adsorption reactions are relevant for prebiotic chemistry. Regarding thermodynamics, adsorption enthalpies should be negative, or the biomolecules would have "nothing to say" to the mineral surfaces, but not *too* negative, lest the peptides possibly formed on these surfaces remain trapped on them. In a criticism of the involvement of surfaces in prebiotic chemistry, de Duve and Miller once feared that it would lead to "a dead end, in which the surface is covered by molecules so tightly bonded that they cannot be further displaced" [96]. The $\Delta_{ads}G^{\circ}$ values that we obtained, at -7.1 to -9.0 k_BT, are encouraging as they would hardly be unsurmountable. There are not many high-quality data in the literature for comparison, be they from macroscopic or molecular-level investigations, but a recent work from our group, using methods similar to the present one, found $\Delta_{ads}G^{\circ}$ of -8.9 and -13.2 k_BT for two different tridecapeptide interacting with a gold surface. Other literature values mentioned in this work indicate that the adsorption free enthalpies remain rather small in absolute value even for rather long peptides. A consequence of that fact must be underlined: the formation of peptides from monomeric amino

acids that has been observed on alumina (among other surfaces) is not only due to a thermodynamic stabilization of the reaction products (the peptides) following their adsorption [97,98].

From the kinetic point of view, it is of high interest to have a method available that allows to compare the kinetic constants for different biomolecule/surface systems. In realistic prebiotic scenarios, chemical phenomena occurring on surfaces between adsorbed molecules are integrated into a series of steps involving adsorption and desorption, and intermediates must remain on the surface from the "right" amount of time in order for the scenario to be viable.

One can also ask what type of adsorption mechanism is involved for peptides on mineral surfaces. It is hard to answer this question from the sole value of $\Delta_{ads}G^{\circ}$; in particular, amino acids adsorption may be entropically driven, and among entropic effects, the changes in the organization of solvent molecules may play a critical role. A few comments may still be offered.

The absolute value of the adsorption enthalpy is about an order of magnitude smaller than the dissociation enthalpy of a typical covalent bond, and this kind of interaction is therefore unlikely. The formation of coordination bonds, such as between the peptide carboxylate groups and Al^{3+}, would be several times less energetic however, and cannot be ruled out. Among weaker interactions, one can consider electrostatic interactions, hydrogen bonding and van der Waals interactions. The Glu-Ala peptide bears a net negative charge at pH 6.8, since the pK_a values for peptide terminal $-$COOH lie in the 2.4 to 3.2 range, and that for the side-chain $-$COOH of Glu is 4.25. On the other hand, our results using the colloidal probe indicate that the AlOx surface is also negatively charged in the adsorption conditions, while that of T-AlOx is on average slightly positively charged (Fig. 6E). Thus, the electrostatic contribution to the peptide/surface interaction should be unfavorable on AlOx, and favorable on T-AlOx, in line with the more favorable $\Delta_{ads}G^{\circ}$ experimentally measured on T-AlOx. However, it is probably not predominant since the difference is only a fraction of the global value. Thus, it is likely that the interaction of the peptide fragment with both aluminic surfaces, as measured at the single-molecule level, can primarily be attributed to a combination of van der Waals forces and hydrogen bonds that stabilize the molecule-surface complex. The combination of these two types of interactions results in a range of forces, depending on the loading rate, that fall within the force spectrum typically observed by SMFS for interactions between biological receptors, where these forces are known to play a major role [99,100].

It is plausible that the organization of hydroxyl groups on the T-AlOx surface leads to a configuration in which the peptide forms more stable hydrogen bonds compared to those formed on the AlOx surface, which could explain the higher absolute value of $\Delta_{ads}G^{\circ}$ observed. In fact, in the rare instances where the interaction of amino acids with mineral surfaces has been investigated at the molecular level, it was found that a specific lattice of H-bonds was formed between the biomolecule and the surface [101,102], which is interesting in view of the widespread importance of specific H-bonding in biochemistry.

The presence of hydrophobic domains on the T-AlOx surface, as demonstrated by chemical force microscopy (Fig. 5F), may also contribute to the interaction, allowing favorable van der Waals interactions with the nonpolar $-CH_3$ group in the peptide molecule.

In order to discriminate between the different contributions of the peptide/surface interactions, it would be interesting to compare Glu-Ala with other peptides, substituting amino acids that have side chains with the ability to interact electrostatically after ionization (Glu, Lys), to form H-bonds (Ser, Tyr), or to interact with hydrophobic patches through non-polar groups (Val, Leu, Ile). Precisely, the methodology developed here provides a robust framework for such investigations, offering a more comprehensive and predictive understanding of the molecular determinants of peptide adsorption on mineral surfaces.

5. Conclusion

This study examines how a small oligopeptide interacts at the single-molecule level with two types of aluminum oxide surfaces: a native oxide formed on a polycrystalline metal substrate (AlOx) and one modified by thermal annealing (T-AlOx). The aim is to assess how chemical changes of the (hydr)oxide affect local surface properties and subsequent peptide interaction. Hydrophobicity and surface charge were first characterized using chemical force microscopy and colloidal probe techniques, respectively. Then, single-molecule force spectroscopy was used to study the interaction of a Glu-Ala dipeptide with both surfaces in aqueous solution. We found that thermal annealing of aluminum substrates induces significant local reorganization of the oxide layer without altering significantly the surface topography. This reorganization leads to a more stoichiometric and structurally ordered Al_2O_3 phase, accompanied by localized surface charge heterogeneity and the emergence of hydrophobic domains.

These nanoscale features directly influence the thermodynamics and kinetics of peptide adsorption. The T-AlOx surface, with its more ordered and chemically heterogeneous interface, supports stronger and more stable peptide binding as evidenced by a significantly lower kinetic off-rate (k_{off}) and higher absolute value of the adsorption free energy ($\Delta_{ads}G^{\circ}$) compared to the native AlOx surface. These findings suggest that the peptide fragment interacts with both AlOx and T-AlOx surfaces primarily through van der Waals forces and hydrogen bonds. Additionally, electrostatic and hydrophobic interactions may contribute to further stabilizing the molecule-surface complex on T-AlOx, whereas the predominantly negatively charged and more disordered AlOx surface results in weaker, less stable interactions.

Our results highlight the importance of accounting for local interfacial properties when evaluating biomolecule–mineral interactions. This insight is crucial not only for designing peptide-functionalized materials with tailored properties and functions, but also for refining hypotheses in the origin-of-life context, where surface-mediated peptide assembly and stabilization may have played a pivotal role. The single-molecule approach employed here offers a valuable framework for scrutinizing complex interfacial phenomena with molecular precision, bridging gaps between surface and colloid science, biophysics, and geochemistry.

Further developments may include an extension of our work to more prebiotically realistic conditions, such as different temperature ranges and aqueous phase composition reflecting seawater or hydrothermal fluids, and studying larger oligopeptides [103].

CRediT authorship contribution statement

Joanne Lê-Chesnais: Writing – review & editing, Writing – original draft, Methodology, Investigation. **Christophe Méthivier:** Writing – review & editing, Investigation. **Daniela Rodriguez:** Writing – review & editing, Investigation, Formal analysis. **Christophe Humbert:** Writing – review & editing, Investigation. **Jean-François Lambert:** Writing – review & editing, Writing – original draft, Validation, Supervision, Methodology, Funding acquisition, Conceptualization. **Jessem Landoulsi:** Writing – review & editing, Writing – original draft, Validation, Supervision, Methodology, Funding acquisition, Conceptualization.

Declaration of competing interest

The authors declare no conflict of interest.

Acknowledgements

The authors thank Alberto Mezzetti for providing access to the ATR-FTIR instrument. The authors acknowledge financial support from the ANR (Pillar ANR-19-CE06-0032). J. Lê-Chesnais acknowledge the financial support of the Ministry of Higher Education, Research and

Innovation (MESRI).

Supplementary materials

Supplementary material associated with this article can be found, in the online version, at doi:10.1016/j.apsadv.2025.100840.

Data availability

Data will be made available on request.

References

[1] S.L. Bellis, Advantages of RGD peptides for directing cell association with biomaterials, Biomaterials 32 (2011) 4205–4210.
[2] I.W. Hamley, Small bioactive peptides for biomaterials design and therapeutics, Chem. Rev. 117 (2017) 14015–14041.
[3] S. Dogan, H. Fong, D.T. Yucesoy, T. Cousin, C. Gresswell, S. Dag, G. Huang, M. Sarikaya, Biomimetic tooth repair: amelogenin-derived peptide enables in vitro remineralization of Human enamel, ACS Biomater. Sci. Eng. 4 (2018) 1788–1796.
[4] H. Lu, M.A. Hood, S. Mauri, J.E. Baio, M. Bonn, R. Muñoz-Espí, T. Weidner, Biomimetic vaterite formation at surfaces structurally templated by oligo (glutamic acid) peptides, Chem. Commun. 51 (2015) 15902–15905.
[5] I.A. Banerjee, L. Yu, H. Matsui, Cu nanocrystal growth on peptide nanotubes by biomineralization: size control of Cu nanocrystals by tuning peptide conformation, Proc. National Acad. Sci. 100 (2003) 14678–14682.
[6] C.-L. Chen, N.L. Rosi, Peptide-based methods for the preparation of nanostructured inorganic materials, Angew. Chem., Int. Ed. Engl. 49 (2010) 1924–1942.
[7] I. Ghosh, J. Chmielewski, Peptide self-assembly as a model of proteins in the pre-genomic world, Curr. Opin. Chem. Biol. 8 (2004) 640–644.
[8] A. Brack, From interstellar amino acids to prebiotic catalytic peptides: a review, Chem. Biodivers. 4 (2007) 665–679.
[9] M. Frenkel-Pinter, M. Samanta, G. Ashkenasy, L.J. Leman, Prebiotic peptides: molecular hubs in the origin of life, Chem. Rev. 120 (2020) 4707–4765.
[10] M. Fishkis, Steps towards the formation of A protocell: the possible role of short peptides, Orig. Life Evol. Biosph. 37 (2007) 537–553.
[11] E.J. Milner-White, M.J. Russell, Functional capabilities of the earliest peptides and the emergence of life, Genes 2 (2011) 671–688.
[12] K. Ikehara, [GADV]-protein world hypothesis on the origin of life, Orig. Life Evol. Biosph.: J. Int. Soc. Study Orig. Life 44 (2014) 299–302.
[13] N. Lahav, D. White, S. Chang, Peptide formation in the prebiotic era: thermal condensation of glycine in fluctuating clay environments, Sci. 201 (1978) 67–69.
[14] V.A. Basiuk, T.Y. Gromovoy, V.G. Golovaty, A.M. Glukhoy, Mechanisms of amino acid polycondensation on silica and alumina surfaces, Orig. Life Evol. Biosph., 20 (1990) 483-498.
[15] A.R. Hill, C. Böhler, L.E. Orgel, Polymerization on the rocks: negatively-charged α-amino acids, Orig. Life Evol. Biosph. 28 (1998) 235–243.
[16] G. Martra, C. Deiana, Y. Sakhno, I. Barberis, M. Fabbiani, M. Pazzi, M. Vincenti, The formation and self-assembly of long prebiotic oligomers produced by the condensation of unactivated amino acids on oxide surfaces, Angew. Chem. Int. Ed. 53 (2014) 4671–4674.
[17] Y. Sakhno, A. Battistella, A. Mezzetti, M. Jaber, T. Georgelin, L. Michot, J.-F. Lambert, One step up the ladder of prebiotic complexity: formation of nonrandom linear polypeptides from binary systems of amino acids on silica, Chem.–A Eur. J. 25 (2019) 1275–1285.
[18] L. Bedoin, S. Alves, J.-F. Lambert, Origins of life and molecular information: selectivity in mineral surface-induced prebiotic amino acid polymerization, ACS Earth Space Chem. 4 (2020) 1802–1812.
[19] R.M. Hazen, Paleomineralogy of the Hadean Eon: a preliminary species list, American J. Sci. 313 (2013) 807–843.
[20] J. Bujdak, B.M. Rode, Preferential amino acid sequences in alumina-catalyzed peptide bond formation, J. inorg. bio. 90 (2002) 1–7.
[21] J. Bujdák, B.M. Rode, Calorimetry, alumina catalyzed reactions of amino acids, J. Ther. Analy. Cal. 73 (2003) 797–805.
[22] J. Bujdák, B.M. Rode, Silica, alumina, and clay-catalyzed alanine peptide bond formation, J. mol. evol. 45 (1997) 457–466.
[23] J. Bujdák, B.M. Rode, Glycine oligomerization on silica and alumina, React. Kinet. Catal. Lett. 62 (1997) 281–286.
[24] V.A. Basiuk, T.Y. Gromovoy, Reactions of vaporous proteinogenic α-amino acids on silica and alumina surfaces, React. Kinet. Catal. Lett. 50 (1993) 297–303.
[25] I. Lopes, L. Piao, L. Stievano, J.-F. Lambert, Adsorption of amino acids on oxide supports: a solid-state NMR study of glycine adsorption on silica and alumina, J. Phys. Chem. 113 (2009) 18163–18172.
[26] M. Bouchoucha, M. Jaber, T. Onfroy, J.-F. Lambert, B. Xue, Glutamic acid adsorption and transformations on silica, J. Phys.l Chem. C 115 (2011) 21813–21825.
[27] M. Digne, P. Sautet, P. Raybaud, H. Toulhoat, E. Artacho, Structure and stability of aluminum hydroxides: a theoretical study, J. Phys. Chem. B 106 (2002) 5155–5162.
[28] J.L. Bañuelos, E. Borguet, G.E. Brown Jr., R.T. Cygan, J.J. DeYoreo, P.M. Dove, M.-P. Gaigeot, F.M. Geiger, J.M. Gibbs, V.H. Grassian, A.G. Ilgen, Y.-S. Jun, N. Kabengi, L. Katz, J.D. Kubicki, J. Lützenkirchen, C.V. Putnis, R.C. Remsing, K. M. Rosso, G. Rother, M. Sulpizi, M. Villalobos, H. Zhang, Oxide– and silicate–water interfaces and their roles in technology and the environment, Chem. Rev. 123 (2023) 6413–6544.
[29] M. Trueba, S.P. Trasatti, γ-Alumina as a support for catalysts: a review of fundamental aspects, Eur. J. Inorg. Chem. 2005 (2005) 3393–3403.
[30] B. Zhou, B. Bai, X. Zhu, J. Guo, Y. Wang, J. Chen, Y. Peng, W. Si, S. Ji, J. Li, Insights into effects of grain boundary engineering in composite metal oxide catalysts for improving catalytic performance, J. Colloid. Interface Sci. 653 (2024) 1177–1187.
[31] S. Cao, N. Sui, P. Zhang, T. Zhou, J. Tu, T. Zhang, TiO2 nanostructures with different crystal phases for sensitive acetone gas sensors, J. Colloid. Interface Sci. 607 (2022) 357–366.
[32] J. Landoulsi, Surface (bio)-functionalization of metallic materials: how to cope with real interfaces? Adv. Colloid. Interface Sci. 325 (2024) 103054.
[33] P. Steinbauer, A. Rohatschek, O. Andriotis, N. Bouropoulos, R. Liska, P. J. Thurner, S. Baudis, Single-molecule force spectroscopy reveals adhesion-by-demand in statherin at the protein–hydroxyapatite interface, Langmuir 36 (2020) 13292–13300.
[34] Y. Li, J. Cheng, P. Delparastan, H. Wang, S.J. Sigg, K.G. DeFrates, Y. Cao, P. B. Messersmith, Molecular design principles of Lysine-DOPA wet adhesion, Nat. Commun. 11 (2020) 3895.
[35] A. Fuhrmann, R. and Ros, Single-molecule force spectroscopy: a method for quantitative analysis of ligand–Receptor interactions, Nanomedicine 5 (2010) 657–666.
[36] J. Zuo, H. Chen, H. Li, Two molecule force spectroscopy on ligand–receptor interactions, Nanoscale 15 (2023) 16581–16589.
[37] C.J. Newcomb, N.P. Qafoku, J.W. Grate, V.L. Bailey, J.J. De Yoreo, Developing a molecular picture of soil organic matter–mineral interactions by quantifying organo–mineral binding, Nat. Commun. 8 (2017) 396.
[38] H. Zhai, W. Zhang, L. Wang, C.V. Putnis, Dynamic force spectroscopy for quantifying single-molecule organo–mineral interactions, CrystEngComm 23 (2021) 11–23.
[39] J. Landoulsi, V. Dupres, Probing peptide–inorganic surface interaction at the single molecule level using force spectroscopy, Chem. Phys. Chem. 12 (2011) 1310–1316.
[40] Y. Arai, K.-I. Okabe, H. Sekiguchi, T. Hayashi, M. Hara, Nanoscale Chemical composition analysis using peptides targeting inorganic materials, Langmuir 27 (2011) 2478–2483.
[41] A. Pohl, F. Berger, R.M.A. Sullan, C. Valverde-Tercedor, K. Freindl, N. Spiridis, C. T. Lefèvre, N. Menguy, S. Klumpp, K.G. Blank, D. Faivre, Decoding biomineralization: interaction of a Mad10-derived peptide with magnetite thin films, Nano Lett. 19 (2019) 8207–8215.
[42] J. Zhang, L. Wang, W. Zhang, C.V. Putnis, Phosphorylated/nonphosphorylated motifs in amelotin turn off/on the acidic amorphous calcium phosphate-to-apatite phase transformation, Langmuir 36 (2020) 2102–2109.
[43] R. Afrin, T.-a. Yano, T.Z. Jia, H.J. Cleaves, M. Hara, Unbinding events of amino acids and peptides from water–pyrite interfaces: a case study of life's origin on mineral surfaces, Biophys. Chem. 260 (2020) 106338.
[44] G.I. Bell, Models for the specific adhesion of cells to cells, Science 200 (1978) 618–627.
[45] E. Evans, K. Ritchie, Strength of a weak bond connecting flexible polymer chains, Biophys. J. 76 (1999) 2439–2447.
[46] C. Jarzynski, Equilibrium free-energy differences from nonequilibrium measurements: a master-equation approach, Phys. Rev. E 56 (1997) 5018–5035.
[47] G. Hummer, A. Szabo, Free energy reconstruction from nonequilibrium single-molecule pulling experiments, Proc. Natl. Acad. Sci. 98 (2001) 3658–3661.
[48] J. Lê-Chesnais, M. Steffenhagen, C. Méthivier, D. Costa, D. Rodriguez, J.-F. Lambert, E. Maisonhaute, J. Landoulsi, Binding mechanism of oligopeptides on solid surface: assessing the significance of single-molecule approach, Nanoscale (2025).
[49] A. Leader, D. Mandler, M. Reches, The role of hydrophobic, aromatic and electrostatic interactions between amino acid residues and a titanium dioxide surface, Phys. Chem. Chem. Phys. 20 (2018) 29811–29816.
[50] S. Maity, D. Zanuy, Y. Razvag, P. Das, C. Alemán, M. Reches, Elucidating the mechanism of interaction between peptides and inorganic surfaces, Phys. Chem. Chem. Phys. 17 (2015) 15305–15315.
[51] W.-S. Choe, M.S.R. Sastry, C.K. Thai, H. Dai, D.T. Schwartz, F. Baneyx, Conformational control of inorganic adhesion in a designer protein engineered for cuprous oxide binding, Langmuir 23 (2007) 11347–11350.
[52] J. Landoulsi, V. Dupres, C. Méthivier, I.L. Mfiban, P. Cornette, E. Colaço, C.-M. Pradier, Surface-generated copper ions induce multilayer growth of small peptides, Appl. Surf. Sci. 507 (2020) 145105.
[53] D.A. Zaia, C.T.B. Zaia, H. De Santana, Which amino acids should be used in prebiotic chemistry studies? Orig. Life Evol. Biosph. 38 (2008) 469–488.
[54] S. Villafañe-Barrajas, J.F. Lambert, Unpublished results.
[55] A. Ebner, L. Wildling, A.S.M. Kamruzzahan, C. Rankl, J. Wruss, C.D. Hahn, M. Hölzl, R. Zhu, F. Kienberger, D. Blaas, P. Hinterdorfer, H.J. Gruber, A. New, Simple method for linking of antibodies to atomic force microscopy tips, Bioconjug. Chem. 18 (2007) 1176–1184.
[56] N. Fairley, V. Fernandez, M. Richard-Plouet, C. Guillot-Deudon, J. Walton, E. Smith, D. Flahaut, M. Greiner, M. Biesinger, S. Tougaard, D. Morgan, J. Baltrusaitis, Systematic and collaborative approach to problem solving using X-ray photoelectron spectroscopy, Appl. Surf. Sci. Adv. 5 (2021) 100112.

[57] C. Humbert, O. Pluchery, E. Lacaze, A. Tadjeddine, B. Busson, Optical spectroscopy of functionalized gold nanoparticles assemblies as a function of the surface coverage, Gold. Bull. 46 (2013) 299–309.
[58] Gouy, Sur la constitution de la charge électrique à la surface d'un électrolyte, J. Phys. Theor. Appl. 9 (1910) 457–468.
[59] D.L. Chapman, LI, A contribution to the theory of electrocapillarity, Lond. Edinb. Dublin Philos. Mag. J. Sci. 25 (1913) 475–481.
[60] O. Stern, Zur theorie der elektrolytischen doppelschicht, Zeitschrift für Elektrochemie und angewandte physikalische Chemie 30 (1924) 508–516.
[61] L.L.D. Derjaguin B, Theory of the stability of strongly charged lyophobic sols and of the adhesion of strongly charged particles in solutions of electrolytes, Acta Physicochim. U.R.S.S. 14 (1941) 633–662.
[62] E.J. Verwey, Theory of the stability of lyophobic colloids, J. Phys. Colloid. Chem. 51 (1947) 631–636.
[63] X. Yin, J. Drelich, Surface charge microscopy: novel technique for mapping charge-mosaic surfaces in electrolyte solutions, Langmuir 24 (2008) 8013–8020.
[64] I. Larson, C.J. Drummond, D.Y.C. Chan, F. Grieser, Direct force measurements between silica and alumina, Langmuir 13 (1997) 2109–2112.
[65] R.W. Friddle, A. Noy, J.J. De Yoreo, Interpreting the widespread nonlinear force spectra of intermolecular bonds, Proc. Natl. Acad. Sci. 109 (2012) 13573–13578.
[66] M. Arrar, F.M. Boubeta, M.E. Szretter, M. Sued, L. Boechi, D. Rodriguez, On the accurate estimation of free energies using the Jarzynski equality, J. Comput. Chem. 40 (2019) 688–696.
[67] Z. Kuang, K.M. Singh, D.J. Oliver, P.B. Dennis, C.C. Perry, R.R. Naik, Gamma estimator of Jarzynski equality for recovering binding energies from noisy dynamic data sets, Nat. Commun. 11 (2020) 5517.
[68] B. Foley, C. Méthivier, A. Miche, S. Guira, L. Valentin, K. El Kirat, C. Guibert, J. Landoulsi, Unveiling the composition of hydroxyapatite minerals and their (bio)-organic adlayer using X-ray photoelectron spectroscopy, Appl. Surf. Sci. 647 (2024) 158577.
[69] A.G. Shard, B.P. Reed, D.J.H. Cant, Surface analysis insight note: uncertainties in XPS elemental quantification, Surf. Interface Anal. 57 (2025) 389–395.
[70] K. Wefers, C. Misra, Oxides and Hydroxides of Aluminum, Alcoa Research Laboratories, 1987.
[71] J. van den Brand, O. Blajiev, P.C.J. Beentjes, H. Terryn, J.H.W. de Wit, Interaction of anhydride and carboxylic acid compounds with aluminum oxide surfaces studied using infrared reflection absorption spectroscopy, Langmuir 20 (2004) 6308–6317.
[72] J. van den Brand, O. Blajiev, P.C.J. Beentjes, H. Terryn, J.H.W. de Wit, Interaction of ester functional groups with aluminum oxide surfaces studied using infrared reflection absorption spectroscopy, Langmuir 20 (2004) 6318–6326.
[73] A.B. Kiss, G. Keresztury, L. Farkas, Raman and ir spectra and structure of boehmite (γ-AlOOH). Evidence for the recently discarded D172h space group, Spectrochimica Acta Part A: Mol. Spectrosc. 36 (1980) 653–658.
[74] Z. Wang, J. Gong, J. Ma, J. Xu, In situ growth of hierarchical boehmite on 2024 aluminum alloy surface as superhydrophobic materials, RSC Adv. 4 (2014) 14708–14714.
[75] V.J. Ingram-Jones, R.C.T. Slade, T.W. Davies, J.C. Southern, S. Salvador, Dehydroxylation sequences of gibbsite and boehmite: study of differences between soak and flash calcination and of particle-size effects, J. Mater. Chem. 6 (1996) 73–79.
[76] C. Su, D.L. Suarez, Situ infrared speciation of adsorbed carbonate on aluminum and iron oxides, Clays Clay Min. 45 (1997) 814–825.
[77] G. Busca, The surface of transitional aluminas: A critical review, Catal. Today 226 (2014) 2–13.
[78] L. Zhang, C. Tian, G.A. Waychunas, Y.R. Shen, Structures and charging of α-alumina (0001)/water interfaces studied by sum-frequency vibrational spectroscopy, J. Am. Chem. Soc. 130 (2008) 7686–7694.
[79] J. Sung, L. Zhang, C. Tian, Y.R. Shen, G.A. Waychunas, Effect of pH on the water/α-Al2O3 (11¯02) interface structure studied by sum-frequency vibrational spectroscopy, J. Phys. Chem. C 115 (2011) 13887–13893.
[80] A.L. Barabási, H.E. Stanley, Fractal Concepts in Surface Growth; Cambridge University Press: Cambridge, U.K, 1995, Cambridge University Press, Cambridge, U.K, 1995.
[81] M. Beauvais, I. Liascukiene, A.M. Jonas, J. Landoulsi, Fatty acid monolayers on randomly nanostructured inorganic surfaces: interplay of wettability, chemistry, and topography, Langmuir 36 (2020) 11845–11854.
[82] Y. Gan, G.V. Franks, Charging behavior of the gibbsite basal (001) surface in NaCl solution investigated by AFM colloidal probe technique, Langmuir 22 (2006) 6087–6092.
[83] S. Veeramasuneni, M.R. Yalamanchili, J.D. Miller, Measurement of interaction forces between silica and α-alumina by Atomic force microscopy, J. Colloid. Interface Sci. 184 (1996) 594–600.
[84] G.V. Franks, L. Meagher, The isoelectric points of sapphire crystals and alpha-alumina powder, Colloids Surf. A: Physicochem. Eng. Asp. 214 (2003) 99–110.
[85] A.G. Stack, S.R. Higgins, C.M. Eggleston, Point of zero charge of a corundum-water interface probed with optical second harmonic generation (SHG) and atomic force microscopy (AFM): new approaches to oxide surface charge, Geochim. Cosmochim. Acta 65 (2001) 3055–3063.
[86] J.P. Fitts, X. Shang, G.W. Flynn, T.F. Heinz, K.B. Eisenthal, Electrostatic surface charge at aqueous/α-Al2O3 single-crystal interfaces as probed by optical second-harmonic generation, J. Phys. Chem. B 109 (2005) 7981–7986.
[87] A. Tulpar, D.B. Henderson, M. Mao, B. Caba, R.M. Davis, K.E. Van Cott, W. A. Ducker, Unnatural proteins for the control of surface forces, Langmuir 21 (2005) 1497–1506.
[88] G.V. Franks, Y. Gan, Charging behavior at the alumina–water interface and implications for ceramic processing, J. American Ceram. Soci. 90 (2007) 3373–3388.
[89] H. Yong, W.H. Van Riemsdijk, Interfacial charging phenomena of aluminum (Hydr)oxides, Langmuir 15 (1999) 5942–5955.
[90] J. Lützenkirchen, A. Abdelmonem, R. Weerasooriya, F. Heberling, V. Metz, R. Marsac, Adsorption of dissolved aluminum on sapphire-c and kaolinite: implications for points of zero charge of clay minerals, Geochem. Trans. 15 (2014) 9.
[91] X. Carrier, E. Marceau, J.-F. Lambert, M. Che, Transformations of γ-alumina in aqueous suspensions: 1. Alumina chemical weathering studied as a function of pH, J. Colloid. Interface Sci. 308 (2007) 429–437.
[92] L.Moreno Ostertag, T. Utzig, C. Klinger, M. Valtiner, Tether-length dependence of bias in equilibrium free-energy estimates for surface-to-molecule unbinding experiments, Langmuir 34 (2018) 766–772.
[93] R. Hazen, Paleomineralogy of the Hadean Eon: a preliminary species list, Am. J. Sci. 313 (2013) 807–843.
[94] V.A.C. Haanappel, H.D. van Corbach, T. Fransen, P.J. Gellings, The effect of thermal annealing on the properties of alumina films prepared by metal organic chemical vapour deposition at atmospheric pressure, Surf. Coat. Technol. 64 (1994) 183–193.
[95] A.C. Dillon, A.W. Ott, J.D. Way, S.M. George, Surface chemistry of Al2O3 deposition using Al(CH3)3 and H2O in a binary reaction sequence, Surf. Sci. 322 (1995) 230–242.
[96] C. de Duve, S.L. Miller, Two-dimensional life? Proc. Natl. Acad. Sci. U.S.A. 88 (1991) 10014–10017.
[97] K. Marshall-Bowman, S. Ohara, D.A. Sverjensky, R.M. Hazen, H.J. Cleaves, Catalytic peptide hydrolysis by mineral surface: implications for prebiotic chemistry, Geochim. Cosmochim. Acta 74 (2010) 5852–5861.
[98] J.-F. Lambert, L. Ter-Ovanessian, M.-C. Maurel, Studies in mineral-assisted protometabolisms, First Steps Life (2024) 193–215.
[99] P. Hinterdorfer, Y.F. Dufrêne, Detection and localization of single molecular recognition events using atomic force microscopy, Nat. Methods 3 (2006) 347–355.
[100] D.J. Müller, Y.F. Dufrêne, Atomic force microscopy as a multifunctional molecular toolbox in nanobiotechnology, Nat. Nanotechnol. 3 (2008) 261–269.
[101] O.E. Samrout, G. Berlier, J.-F. Lambert, Amino acid polymerization on silica surfaces, ChemPlusChem 89 (2024) e202300642.
[102] H. Abadian, P. Cornette, D. Costa, A. Mezzetti, C. Gervais, J.F. Lambert, Leucine on silica: a combined experimental and modeling study of a system relevant for origins of life, and the role of water coadsorption, Langmuir 38 (2022) 8038–8053.
[103] R. Afrin, N. Ganbaatar, M. Aono, H.J. Cleaves Li, T.A. Yano, M. Hara, Size-dependent affinity of glycine and its short oligomers to pyrite surface: a model for prebiotic accumulation of amino acid oligomers on a mineral surface, Int. j. Mol. Sci. 19 (2018) 365.